JGR Oceans

RESEARCH ARTICLE
10.1029/2018JC014655

Meridional Heat and Salt Transport Across the Subantarctic Front by Cold-Core Eddies

Ramkrushnbhai S. Patel[1,2], **Helen E. Phillips**[1,3], **Peter G. Strutton**[1,3], **Andrew Lenton**[4,5,6], **and Joan Llort**[1,2]

[1]Institute for Marine and Antarctic Studies, University of Tasmania, Hobart, Tasmania, Australia, [2]Australian Research Council Center of Excellence for Climate System Science, University of Tasmania, Hobart, Tasmania, Australia, [3]Australian Research Council Center of Excellence for Climate Extremes, University of Tasmania, Hobart, Tasmania, Australia, [4]Commonwealth Scientific and Industrial Research Organisation Oceans and Atmosphere, Castray Esplanade, Hobart, Tasmania, Australia, [5]Antarctic Climate and Ecosystems Cooperative Research Centre, University of Tasmania, Hobart, Tasmania, Australia, [6]Centre for Southern Hemisphere Oceans Research, CSIRO, Castray Esplanade, Hobart, Tasmania, Australia

Key Points:
- We characterize for the first time the physical structure of a Subantarctic Front cold-core eddy, south of Tasmania in the Southern Ocean
- Long-lived cold-core eddies transport about 21% of the required meridional heat flux across the Subantarctic Front
- Previous studies have underestimated the total heat and salt content transport by cold-core eddies due to limited observations

Correspondence to:
R. Patel,
Ramkrushnbhai.Patel@utas.edu.au

Citation:
Patel, R. S., Phillips, H. E., Strutton, P. G., Lenton, A., & Llort, J. (2019). Meridional heat and salt transport across the Subantarctic Front by cold-core eddies. *Journal of Geophysical Research: Oceans*, *124*, 981–1004. https://doi.org/10.1029/2018JC014655

Received 10 OCT 2018
Accepted 22 JAN 2019
Accepted article online 28 JAN 2019
Published online 12 FEB 2019

Abstract Mesoscale eddies are ubiquitous in the Southern Ocean particularly in regions where the Antarctic Circumpolar Current interacts with topography. Eddies play a critical role in the meridional transport of heat and salt across the Antarctic Circumpolar Current. However, observations of the heat and salt content of eddies are extremely rare. Here we present new observations that characterize the three-dimensional structure of a cyclonic (cold-core) eddy generated at the Subantarctic Front south of Tasmania. Automated detection software is used with satellite altimetry to follow the eddy through the Subantarctic Zone. The physical properties at the center of the eddy are substantially modified from those near the formation region, indicating a strong transformation during the eddy's lifetime. The eddy carried heat and salt content anomalies relative to surrounding Subantarctic Zone waters of $-0.5 \pm 0.1 \times 10^{20}$ J and $-2.1 \pm 0.4 \times 10^{12}$ kg, respectively. Previous studies have not captured the full heat and salt content of eddies due to limited observations and have underestimated their content by a factor of 2 to 3 south of Tasmania. Applying the observed correlation between eddy-elevated volume and eddy heat and salt content to the history of cyclonic eddies in the satellite altimeter record leads us to propose that about 21% of the heat carried across the Subantarctic Front south of Tasmania is achieved by cyclonic eddies entering the Subantarctic Zone. The freshwater contribution to the Subantarctic Zone by long-lived cold-core eddies is of the same order of magnitude as the Ekman flux in this region.

Plain Language Summary Eddies are rotating bodies of water with diameters between 10 and 100 km that live from a week to months in the ocean. They are known to carry heat and salt across the Antarctic Circumpolar Current. Because of extremely limited direct observations of these eddies, it is difficult to calculate the actual amount of heat and salt that these eddies carry. Here we present new observations of a cold-core eddy that we sampled during a voyage in the Southern Ocean south of Tasmania. The eddy was born in the Subantarctic Front and traveled into the Subantarctic Zone where it stayed for 2 months before returning to the Subantarctic Front and disappearing. The observations showed that the amount of heat carried into the Subantarctic Zone is 2.6 times higher than previously reported, and the amount of salt is 2.5 times larger for south of Tasmania. Based on our in situ observations, combined with satellite measurements of sea surface height and an eddy-tracking software, we propose that 21% of the heat carried across the Subantarctic Front south of Tasmania is achieved by long-lived, cold-core eddies entering the Subantarctic Zone.

1. Introduction

Mesoscale eddies are coherent, rotating bodies of water with diameters of $O(10–100)$ km and life cycles of weeks to months. They assume a central role in the meridional exchange of heat and salt of the Southern Ocean (SO) because there is no mean meridional geostrophic flow across the Antarctic Circumpolar Current (ACC) at the depths shallower than the ocean ridges (Rintoul et al., 2001; Rintoul & Naveira Garabato, 2013). This absence of a mean flow contributes to preserving the cold climate of Antarctica and the high-latitude

SO (Rintoul et al., 2001; Rintoul & Naveira Garabato, 2013). To maintain the heat and salt balance of the SO requires a southward transport by the ocean of approximately 0.3–0.7 PW of heat and 11×10^6 kg/s of salt (Keffer & Holloway, 1988; Lumpkin & Speer, 2007). De Szoeke and Levine (1981) postulated that mesoscale eddies are the most likely candidate to accomplish the required cross-frontal transport. Since de Szoeke and Levine's (1981) postulation, there has been ongoing research into the processes by which these poleward fluxes are achieved examining the relative contributions of time-varying mean flow and transient and standing eddies. For example, Volkov et al. (2010) highlighted the importance of the time-mean field of meridional velocity and potential temperature fluctuations in the poleward meridional heat transport. Ferrari et al. (2014) demonstrated using a model and current meter mooring observations that 80% of the poleward flux of heat was by the mean flow and only 20% by eddies in Drake Passage. In this paper, we aim to quantify the role of transient eddies in the poleward transport of heat and salt across the Subantarctic Front (SAF) in south of Tasmania.

Satellite altimetry has identified the ubiquity of eddies and allowed the characterization of their surface expression across the world ocean (Chelton et al., 2007, 2011). Eddies are nonuniformly distributed throughout the SO, being concentrated near significant topographic obstructions in the path of the ACC where standing meanders are found (Frenger et al., 2015; Morrow et al., 2004). Model studies and altimeter observations have shown the importance of these eddy hotspot regions for the meridional transport of heat and salt across ACC fronts (Dufour et al., 2015; Sallee et al., 2011; Thompson & Sallée, 2012). Foppert et al. (2017) used 4 years of in situ measurements of eddy heat flux (EHF) from C-PIES and a tall mooring in Drake Passage combined with satellite altimeter data to define a proxy for EHF based on sea surface height (SSH) standard deviation and tested the proxy circumpolarly using the SO State Estimate (Mazloff et al., 2010). Using 23.5 years of altimetry observations they mapped the circumpolar distribution of EHF across each jet of the ACC, finding eight regions of elevated poleward heat flux. Interestingly, the heat flux does not cross the full ACC in any one location but is carried zonally and steps southward across each front as it encounters different hotspots along its circumpolar path. These eddy hotspots have also been found to be the locations along the ACC where there is enhanced upwelling of deep waters (Tamsitt et al., 2017).

The EHF estimates of Foppert et al. (2017) agree well with the few in situ estimates from moorings south of Tasmania (Phillips & Rintoul, 2000) and in Drake Passage (Ferrari et al., 2014; Watts et al., 2016). Observations from these moored arrays indicate poleward EHFs of 15.4 kW/m^2 in the Drake Passage (Johnson & Bryden, 1989) and 11.3 kW/m^2 south of Tasmania (Phillips & Rintoul, 2000). These estimates translate to poleward heat fluxes of 1.2 and 0.9 PW, respectively, when extrapolated circumpolarly, which is large enough to balance the heat lost to the atmosphere around Antarctica. However, we have low confidence in these estimates because they are based on measurements in locations of high eddy energy and do not account for the vast regions along the ACC where there is much weaker eddy activity. The circumpolar EHFs across the ACC estimated by Foppert et al. (2017) that do account for zonal variations in fluxes, range from 1.06 PW entering the SAF to 0.24 PW exiting the Polar Front (PF), lower than the aforementioned coarse estimate of 0.9 to 1.2 PW from point measurements. The satellite proxy of Foppert et al. (2017) presents an exciting observational tool to monitor spatial and temporal variations in eddy fluxes, but we need to build confidence in the proxy by validating against in situ measurements of the heat exchange by mesoscale eddies.

Several hydrographic studies have provided direct observations of the heat and salt content of mesoscale eddies. For instance, Joyce et al. (1981) studied a cold-core eddy spawned from an equatorward meander of the Antarctic PF in the Drake Passage, Swart et al. (2008) studied a cold-core eddy formed in the PF south of Africa, and Morrow et al. (2004) exploited existing repeat hydrographic transects along the SR3 line and satellite observations, to explain the formation and propagation of eddies and provided the first estimate of the heat and salt transport by cold-core SAF eddies south of Tasmania. However, this estimate of heat and salt transport may be biased low by incomplete sampling of the horizontal or vertical extent of the eddies that were sampled in these studies.

In this study, we focus on the SO south of Tasmania, a region of moderate but growing eddy kinetic energy downstream of the southward shift of the Southeast Indian Ridge where the ACC becomes free of bathymetric constraint (Phillips & Rintoul, 2000). It is the location of one of four standing meanders that are central to the momentum balance of the ACC (Thompson & Naveira Garabato, 2014). It is also a region where almost 30% of the circumpolar heat transfer across the SAF and PF is estimated to occur (Foppert et al., 2017, their Figure 7).

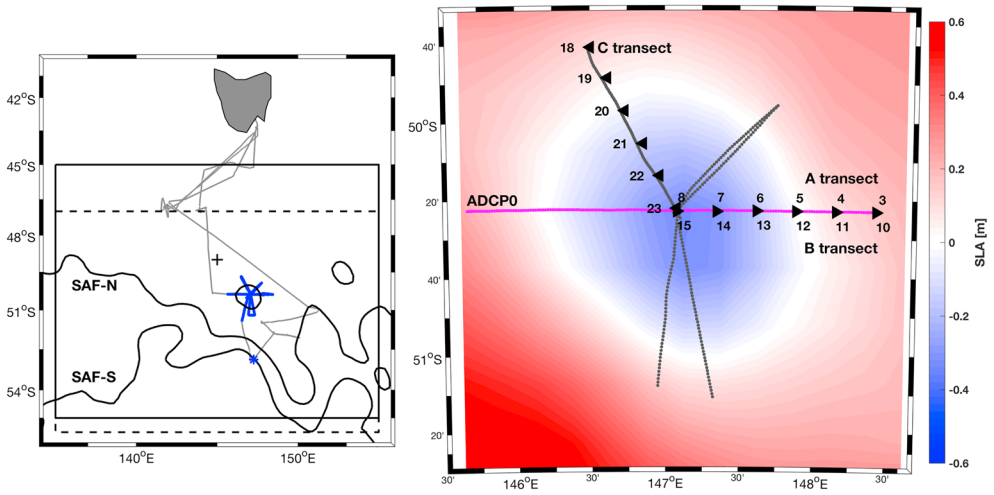

Figure 1. (left) Voyage track of IN2016_V02 (gray lines) and track during the eddy sampling (blue lines); conductivity-temperature-depth cast taken in the Subantarctic Front (blue asterisk); mean positions of the northern and southern branches of the Subantarctic Front during the sampling period (black contours); approximate location of Morrow et al.'s (2004) eddy (black +). Solid black box defines region over which eddy demography was conducted. Dashed line box defines limits for calculation of the eddy heat flux based on Foppert et al. (2017). (right) The radial transects of the eddy sampling, overlaid on the mean sea level anomaly during the sampling period. Dotted lines signify shipboard acoustic Doppler current profiler transects across the eddy (full-diameter transect, ADCP0, highlighted in magenta), where dots denote positions of 5-min average measurement. Triangles indicate conductivity-temperature-depth casts of transects A, B, and C, labeled by cast number. ADCP = acoustic Doppler current profiler; SAF = Subantarctic Front; SLA = sea level anomaly.

We present an unprecedented hydrographic survey of a cyclonic, cold-core, eddy south of Tasmania allowing us to characterize its physical structure and evolution over its lifetime, as well as its heat and salt content. The targeted cold-core eddy formed in the SAF south of Tasmania in February 2016, transited into the Subantarctic Zone (SAZ) where it spent 2 months and was eventually reabsorbed into the SAF in May 2016 (see Figure 1 [left] and 2). In this paper, we first describe the temporal variability of the eddy's characteristics using remotely sensed data employing automated eddy detection and tracking software. We then characterize the physical and dynamical structure of the eddy from in situ observations. Lastly, we calculate the available heat and salt anomalies in the eddy and extend these results using satellite altimetry to estimate the total amount of heat carried across the SAF by cold-core eddies.

2. Data and Methods

2.1. In Situ Observations

We undertook an intensive survey of the physical and biogeochemical structure of a cyclonic, cold-core eddy in the SAZ south of Tasmania (Figure 1, left) over the course of 7 days (30 March to 5 April 2016) from Australia's research vessel RV Investigator, Voyage IN2016_V02. During this survey, we collected 18 conductivity-temperature-depth (CTD) profiles of temperature, salinity, nutrients, and dissolved oxygen concentration from the sea surface to 1,500 dbar (Figure 1, right). All profiles were taken with a Seabird SBE911 CTD 20, which was calibrated for salinity and dissolved oxygen with Niskin bottle water samples at 12 depths on each cast. Water samples from 24 depths were analyzed for nutrients.

The CTD spacing was nominally 15 km apart along three radial transects from the edge of the eddy to its center (Figure 1). The eddy moved laterally by only 13 km over the duration of sampling. We take advantage of the relatively short observation period, and the near stationarity of the eddy to combine transects into a snapshot of the eddy structure. To produce a coherent full-diameter transect across the eddy, we combined CTD transects B and C (Table 1) in a way that produces a vertical section from the northwestern edge, to the center, to the eastern edge of the eddy (Figure 1). We estimated the mixed layer depth for the same transect following de Boyer Montégut et al. (2004) using a temperature difference from the sea surface of 0.2 ° C.

A continuously operating 75-kHz shipboard acoustic Doppler current profiler (SADCP) acquired vertical profiles of current speed and direction down to approximately 750-m depth along the ship track.

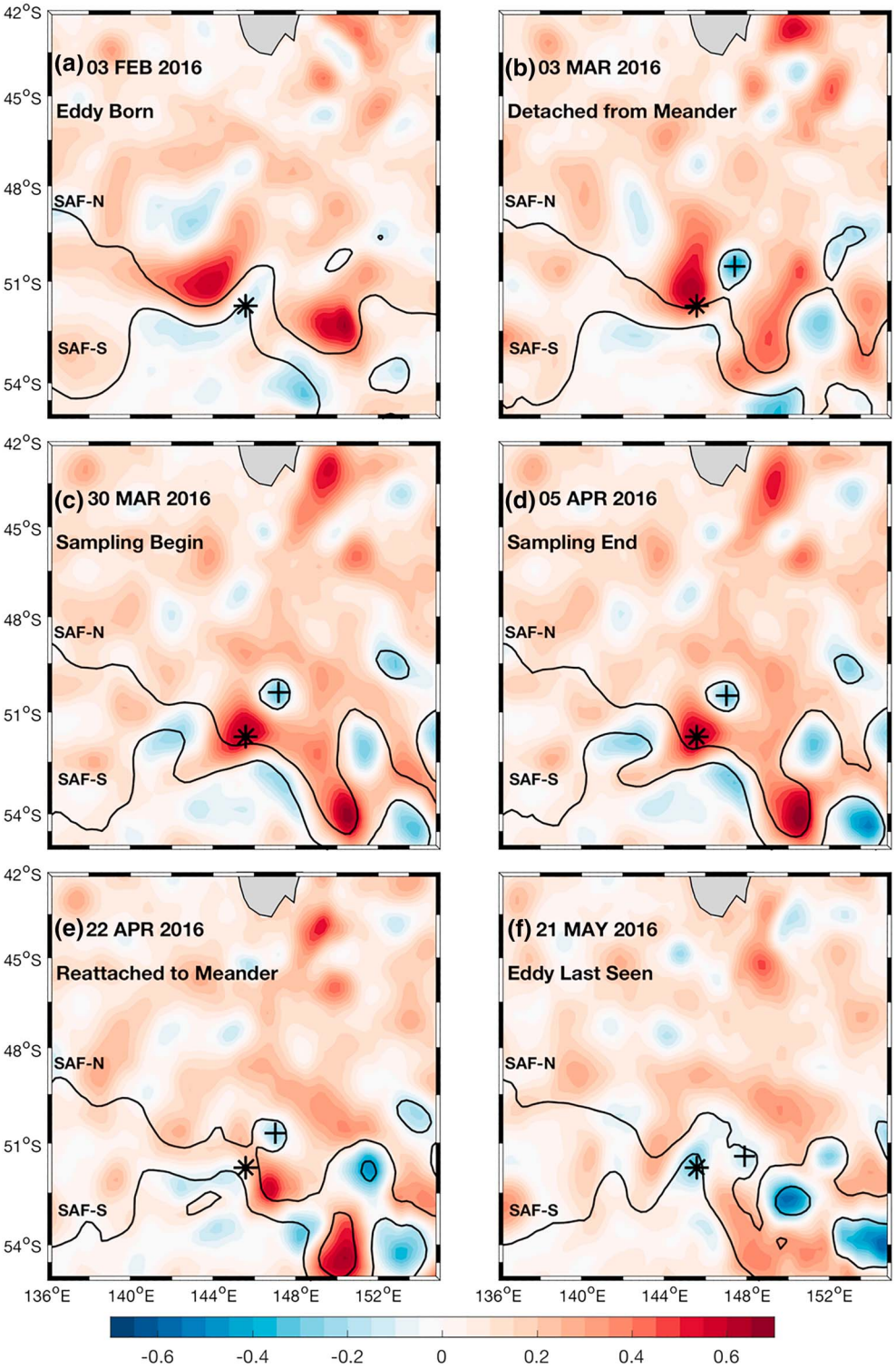

Figure 2. Daily sea level anomaly maps representing the main events of the eddy's life cycle. Black contours represent the northern and southern branches of the Subantarctic Front (SAF-N and SAF-S, respectively), based on absolute dynamic topography of 0.2 and −0.4 m, respectively (Sokolov & Rintoul, 2009). Asterisk represents the center of the eddy at formation, and the plus sign is the center of the eddy at the time of the image, both derived from the eddy-tracking software.

Table 1
Conductivity-Temperature-Depth Casts Sampled in the Cold-Core Eddy and in the Subantarctic Front

Transect	Cast number	Date	Longitude	Latitude	Max pressure
A	3	31-Mar-2016 02:00	148.44° E	50.38° S	1552
	4	31-Mar-2016 05:05	148.16° E	50.38° S	1558
	5	31-Mar-2016 07:57	147.88° E	50.38° S	1554
	6	31-Mar-2016 10:50	147.61° E	50.38° S	1555
	7	31-Mar-2016 13:51	147.35° E	50.38° S	1552
	8	31-Mar-2016 16:40	147.08° E	50.38° S	2254
B	10	01-Apr-2016 07:44	148.42° E	50.38° S	1554
	11	01-Apr-2016 10:51	148.15° E	50.38° S	1554
	12	01-Apr-2016 13:31	147.88° E	50.38° S	1554
	13	01-Apr-2016 16:53	147.61° E	50.38° S	1555
	14	01-Apr-2016 19:52	147.34° E	50.38° S	1556
	15	01-Apr-2016 23:27	147.08° E	50.38° S	1555
C	18	02-Apr-2016 20:05	146.50° E	49.67° S	1552
	19	02-Apr-2016 23:18	146.61° E	49.81° S	1552
	20	03-Apr-2016 02:19	146.73° E	49.95° S	1551
	21	03-Apr-2016 05:04	146.85° E	50.09° S	1552
	22	03-Apr-2016 07:41	146.96° E	50.23° S	1550
	23	03-Apr-2016 10:13	147.07° E	50.37° S	1554
Front	26	06-Apr-2016 04:35	147.26° E	52.87° S	1551

Note. Maximum pressure is measured in decibars. Date is in UTC time zone.

In addition to SADCP data recorded along the three CTD transects, we collected one continuous full-diameter transect (ADCP0) from west to east across the eddy and five radial transects that were uninterrupted by station holding (Figure 1, right). Processing and quality control of the CTD and SADCP data were completed by the data group at Australia's Marine National Facility and are publicly available at https://www.cmar.csiro.au/data/trawler. The ADCP velocities are used to calculate tangential and radial velocity components, which allowed a direct comparison with geostrophic velocities estimated from the CTD profiles. Tangential velocity is defined to be perpendicular to any radius from the center to the edge of the eddy (positive clockwise). Radial velocities indicate movement into or out of the eddy (positive outward).

2.2. Remotely Sensed Observations

We used Archiving, Validation, and Interpretation of Satellite Oceanographic data's (AVISO) gridded sea level anomaly (SLA), geostrophic velocity, and absolute SSH products, taken from the new version of Ssalto/Duacs products disseminated by Copernicus Marine Environment Monitoring Services (CMEMS). The data have a Cartesian 0.25° spatial resolution and daily temporal resolution. The climatology used to compute SLA is based on a 20-year period (1993–2012). We exploited both near-real-time and delayed-mode products of AVISO. The data processing details can be found at https://duacs.cls.fr/.

For satellite chlorophyll and infrared sea surface temperature (SST), we used daily, 9-km-spatial-resolution products from Moderate Resolution Imaging Spectroradiometer-Aqua, disseminated by National Aeronautics and Space Administration (https://oceancolor.gsfc.nasa.gov/). For SST, we also used daily 0.25° -spatial-resolution microwave data from the AMSR-2 instrument (http://www.remss.com/).

We also used the new version of the Roemmich-Gilson Argo Climatology to assess the sensitivity of our reference profile, which is defined in section 2.4. The new version extended Argo-only-derived temperature and salinity fields through 2016. The detail about modification in the new version can be found in Roemmich and Gilson (2009) and at the data portal site, http://sio-argo.ucsd.edu/RG_Climatology.html.

2.3. Eddy Identification and Tracking

Before and during the voyage, we used AVISO near-real-time SLA maps and the Okubo-Weiss (OW) parameter to locate an eddy suitable for sampling. The OW parameter, given by $OW = S_n^2 + S_s^2 - \omega^2$, measures the relative importance of vorticity over strain in fluid flow (Okubo, okubo1970horizontal; Weiss, 1991, 1991). $S_n = U_x - V_y$ is the normal, and $S_s = V_x + U_y$ is the shear component of the strain; $\omega = V_x - U_y$ is the relative vorticity, with the subscripts denoting the partial derivatives in the eastward and northward directions, respectively. The variables U and V are the eastward and northward surface current velocity anomalies, respectively, estimated from SLA using the geostrophic balance.

Negative values of the OW parameter signify the dominance of rotation over deformation, which indicates the presence of an eddy. The relative vorticity sign denotes cyclonic (negative) and anticyclonic (positive) eddies. We followed Frenger et al. (2015) to identify an eddy by filtering $OW < -0.2\sigma_{OW}$, where σ_{OW} denotes the spatial standard deviation of OW. Although OW has several limitations such as underestimating eddy surface area and amplification of noise, it proved an effective tool to identify eddies before and during the voyage. We also compared our results with SST and chlorophyll maps to corroborate the eddy signature. Infrared SST and chlorophyll data were suitable for creating multiple-day or week averages but not useful for real-time eddy-tracking owing to contamination by cloud cover over the SO.

After the voyage, we employed the Faghmous et al. (2015) eddy-tracking software to study the eddy's life cycle and to prepare eddy statistics for our study region. The eddy-tracking software allowed us to track eddies without imposing any expert defined criteria with a detection accuracy of 96.4%. Eddies are dynamic features that move in space at the same time as changing their characteristics in time. Therefore, tracking eddies through time should be completed before applying expert-defined criteria, such as minimum amplitude and diameter, to filter eddies (Faghmous et al., 2014). This software also addresses premature track termination and eddy-merging problems, which were not accounted for in previous detection algorithms (e.g., Chelton et al., 2011). More details on the algorithm, and our amendment to allow regional analysis, are provided in Appendix A.

We applied the eddy-tracking software to daily AVISO SLA maps to detect and track eddies. To identify the center of an eddy, we compared each grid point with 15 neighboring grid points. The outer edge of an eddy was defined by the default threshold of 0.05-cm SLA. We tracked only eddies whose size was ≥16 pixels (~100 km in diameter), allowing them to disappear for 1 day. Then, we analyzed all tracked eddies through animation and identified our eddy. We observed that our eddy signature disappeared on 12 February 2016, 10 days after its formation but reappeared in the subsequent time step. The tracking software interpolated the eddy characteristics across this gap. The amplitude of the eddy was calculated as the difference in magnitude between the estimated basal height of the eddy boundary and the maximum/minimum value of SLA within the eddy. The surface area parameter allows for noncircular eddies as it sums the area of pixels occupied by the eddy. However, to estimate the diameter, a circular shape is assumed and is calculated as $L_e = 2 \cdot \sqrt{A/\pi}$.

To verify the realization of the eddy and corroborate the eddy-tracking software performance, we used animations of SLA, geostrophic velocity, and OW parameter along with the eddy's center positions obtained from the eddy-tracking software. We also tracked the eddy manually following the method used in Pilo et al. (2015). We found that the position of the eddy center was consistent across methods and that the eddy-tracking software produced smoother and more realistic tracks than that of the Pilo et al. (2015) method. The eddy-tracking software also provides the additional information about amplitude, diameter, shape of the eddy, and rotational speed (defined as the mean gesotrophic flow speed within an eddy), while the Pilo et al. (2015) tracking method only returns amplitude and eddy center position.

2.4. Definition of Reference Profile

A reference CTD profile was required to characterize the difference in temperature, salinity, and density inside the eddy relative to the surrounding SAZ waters and to determine the heat and salt content anomalies of the eddy. The choice of reference profile varies in the literature. Examples include, an individual profile outside the eddy (Morrow et al., 2004), a climatological profile (Kurczyn et al., 2013), and a composite reference profile (Joyce et al., 1981; Swart et al., 2008). We defined our reference profile to be the average of the outermost CTD profile on each of the three radial transects (CTDs 3, 10, and 18, see Table 1 and Figures 1 and 5). These three CTDs were well outside the eddy core, and all of them had similar water properties typical of the SAZ environment (Rintoul & Bullister, 1999). The three profiles were located outside the outermost

closed contour of relative vorticity, which coincided with the zero SLA contour, and outside the region of maximum geostrophic velocity.

2.5. Estimation of Heat and Salt Content Anomalies

The method of computing the available heat content anomaly (AHA, in J/m^2) and available salt content anomaly (ASA, in kg/m^2) in an eddy was first implemented by Joyce et al. (1981) for a cyclonic ring in the Drake Passage and subsequently used by other studies (e.g., Morrow et al., 2004, 2003; Swart et al., 2008). Joyce et al. (1981) defined the available heat anomaly of an eddy to be the heat "that is still available after all density surfaces are flattened and subsequently constrained to remain so." They also point out that the available heat anomaly is closely linked to the available salt anomaly because of the requirement of mass conservation. AHA and ASA are calculated for discrete profiles of temperature and salinity inside the eddy and then integrated across the eddy to estimate its total heat and salt content. Density is used as the vertical coordinate to eliminate vertical heave of the isopycnals due to internal waves passing through during sampling. The vertical extent of the eddy must be defined prior to calculating AHA and ASA. We chose a density range 26.5 to 27.5σ_θ, which corresponds to a depth range from the sea surface to ~1,000 m at the center, and ~1,400 m at the edge of the eddy.

Temperature and salinity profiles were first interpolated onto potential density relative to the sea surface, with an interval of 0.02 kg/m^3. We used conservative temperature and absolute salinity (defined in Intergovernmental Oceanographic Commission, 2010; McDougall et al., 2012) in the computation of AHA and ASA, respectively. This allowed us to estimate heat and salt content more accurately and enabled the use of constant specific heat capacity throughout the water column (McDougall & Barker, 2011). For each CTD profile, the AHA (J/m^2) between isopycnal layers σ_i and $\sigma_{i-1} = \sigma_i - 0.1$ kg/m^3 is calculated as

$$AHA_{\sigma_i} = \rho_i C_p h_i [T_{\sigma_i} - T_{\sigma_i}(\text{ref})], \tag{1}$$

where ρ_i is the vertically averaged density between the isopycnals in kilograms per cubic meters; C_p is the specific heat capacity at constant pressure (3,991.9 J/kg/K); h_i is the thickness of the isopycnal layer in meters; T_{σ_i} is the vertically averaged conservative temperature between the isopycnals (° C); T_{σ_i}(ref) is the vertically averaged conservative temperature between the isopycnals from the reference profile (° C).

Likewise, ASA (kg/m^2) between the isopycnals for a given profile is computed as

$$ASA_{\sigma_i} = 0.001 \rho_i h_i [S_{\sigma_i} - S_{\sigma_i}(\text{ref})], \tag{2}$$

where S_{σ_i} is the vertically averaged absolute salinity between the isopycnals in grams per kilogram and S_{σ_i}(ref) is the vertically averaged reference absolute salinity between the isopycnals in grams per kilogram. Here 0.001 converts grams to kilograms.

The cross-diameter structure of the eddy's available heat and salt anomalies is represented as the vertical sum of each profile of AHA and ASA, from the predefined maximum density of the eddy, 27.5 kg/m^3, to the sea surface. The resulting sums ΣAHA (J/m^2) and ΣASA (kg/m^2) are only a function of distance across the eddy. Following Joyce et al. (1981) and Morrow et al. (2003), the total heat and salt content of the eddy relative to its surrounding environment is then defined to be

$$\mathcal{H} = \int_{r=0}^{R} 2\pi r \cdot \Sigma AHA \cdot \mathrm{d}r; \mathcal{S} = \int_{r=0}^{R} 2\pi r \cdot \Sigma ASA \cdot \mathrm{d}r, \tag{3}$$

where dr is the distance between stations, R is the eddy radius, and ΣAHA and ΣASA are vertically summed heat and salt content at a station. The unit of $\mathcal{H}$ is in Joules and of $\mathcal{S}$ is in kilograms.

3. Results

3.1. Life Cycle

We tracked the eddy through its life cycle in maps of SLA (Figure 2). The eddy was first identified as a closed contour of SLA in a meander of the SAF on 3 February 2016 (Figure 2a). The meander steepened over the next month until the eddy detached on 3 March 2016 (Figure 2b), after which the meander relaxed southward and followed a more zonal path. The eddy transited northward in the SAZ to a position near 147° E, 50.5° S, where we surveyed it between 30 March and 5 April 2016. The eddy subsequently moved

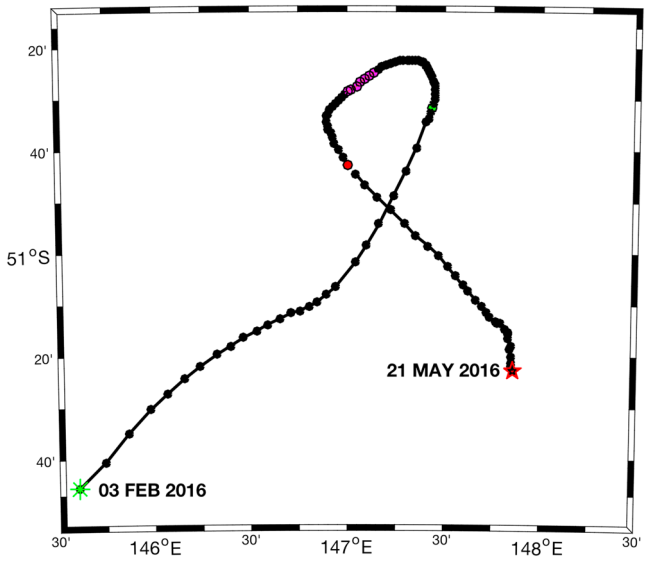

Figure 3. The eddy's track derived from the eddy-tracking software. Each dot represents the detected eddy center each day. Green and red dots delineate detachment from, and reattachment to, the meander, respectively. Magenta dots delineate eddy movement during the sampling period. Green asterisk and red star denote the beginning and end of the track, respectively.

southward again and then reattached to the same meander on 22 April 2016. The eddy remained in the meander until it dissipated on 21 May 2016 (Figures 2e and 2f).

The spatial pattern of the eddy's track is shown in Figure 3. The eddy traveled a total distance of 371 km from formation site to dissipation site at an average propagation speed of 3.4 km/day. Its path consisted of northeast movement for the first 36 days, westward for 16 days, southwestward for 19 days, and then finally southeastward along the meander until it disappeared. The eddy propagated faster before detachment from, and after reattachment to, the meander at speeds of 6.6 and 3.4 km/day, respectively. While separated from the meander, the propagation speed was on average 1.6 km/day. During the sampling period, the eddy was relatively stationary, moving only 11.84 km over 7 days (1.7 km/day).

Eddies tend to experience three phases in their lifetime (Pegliasco et al., 2015). These are the growth phase (which is 20% of the lifetime), mature/stable phase (next 60% of the lifetime), and decay phase (remaining 20% of the lifetime). Dynamical properties such as rotational speed, amplitude, and diameter evolve according to these phases (Pegliasco et al., 2015). Our voyage took place after the eddy had reached its mature stage and had begun to approach its decay phase (Figure 4). During the voyage, rotational speed of the eddy was almost constant while amplitude and diameter of the eddy were decreased gradually (Figure 4).

The evolution of the eddy's dynamical properties during its lifetime is depicted in Figure 4. Amplitude is negative for a Southern Hemisphere cyclonic eddy, but here we refer to the absolute value of the amplitude for simplicity. When the eddy was still trapped in the meander for the first 30 days, its rotational speed, amplitude, and diameter increased

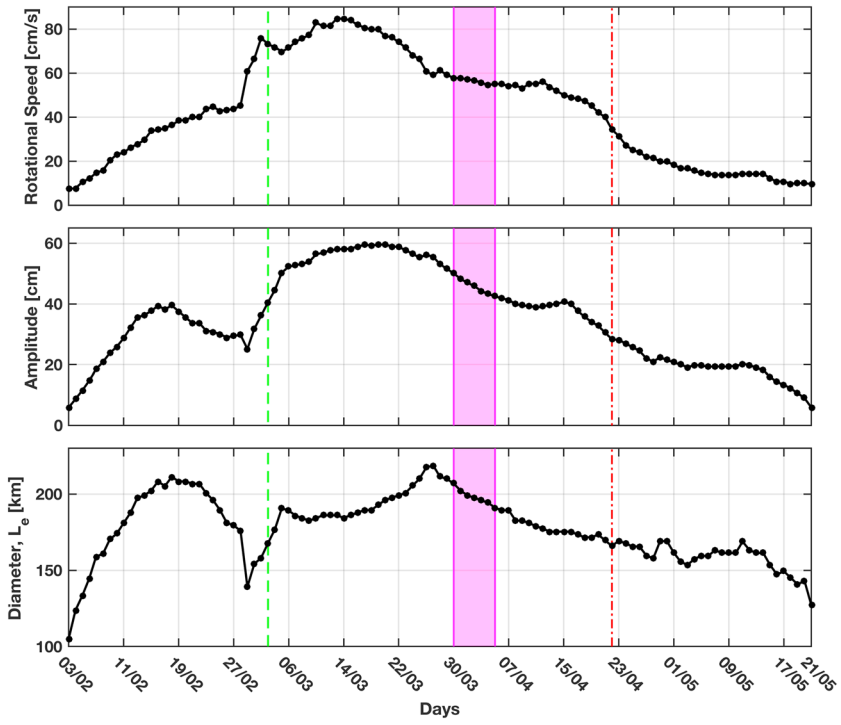

Figure 4. Observed daily rotational speed (top) and amplitude (presented as absolute values, middle panel) and diameter (bottom) over the life span of the eddy. All parameters are the output of the eddy-tracking software. Green vertical dashed line and red vertical dot-dashed line delineate detachment from and reattachment to the meander. Vertical magenta shading defines the sampling period (30 March 2016 to 5 April 2016).

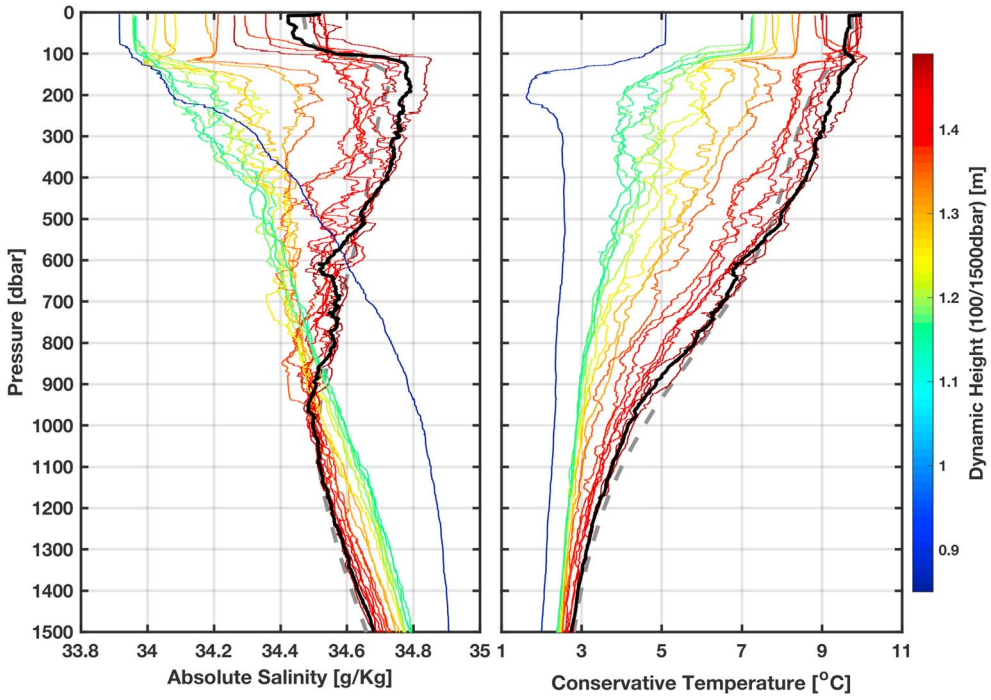

Figure 5. Profiles of absolute salinity (left) and conservative temperature (right) across the eddy and at the Subantarctic Front (where the eddy formed), colored by 100/1,500 dynamic height to illustrate the position of each profile relative to surrounding the Subantarctic Zone waters (red). The Subantarctic Front profile is dark blue. Profiles at the center of the eddy are light green. Black line depicts our reference profile. Gray dashed line indicates March and April climatological reference profile derived from Roemmich and Gilson (2009) Argo climatology.

rapidly (7.5 to 73 cm/s, 5 to 40 cm, and 104 to 205 km, respectively) for the first 15 days. About 2 weeks before the eddy detached, the amplitude and diameter gradually decreased, while the rotational speed continued to increase. Three days before the eddy detached from the meander, there was a rapid increase in all three parameters. The rotation speed slowed as soon as the eddy detached, but the amplitude and diameter continued to increase rapidly for two more days before becoming more steady. Then, rotational speed and amplitude increased gradually and peaked over the next ~15 days to ~84 cm/s and 60 cm, respectively. After the peak, rotational speed and amplitude decreased gradually. Once the eddy reattached to the meander, rotational speed and amplitude decreased rapidly (31 to 9 cm/s and 30 to 5 cm, respectively) over the 30 days from reattachment to dissipation.

The eddy diameter was ~104 km at formation, increasing to a peak of ~218 km on 27 March just prior to sampling and then declining to ~126 km before the eddy dissipated. The median rotational speed and diameter over the life span of the eddy were 43.6 cm/s and 179 km, respectively. Therefore, the angular velocity of the eddy was 4.87×10^{-6} rad/s, which means it would take 14.8 days to complete one revolution. Given that the life span of the eddy was 109 days, it likely would have completed 7.4 revolutions over its life span.

3.2. Physical Properties

Hydrographic profiles of absolute salinity (hereafter, salinity) and conservative temperature (hereafter, temperature) are plotted in Figure 5. They are colored by dynamic height of the 100-dbar pressure surface relative to 1,500 dbar to identify their position relative to the surrounding, higher dynamic height SAZ waters. Dynamic height decreases monotonically from the edge of the eddy to its center and therefore is an excellent indicator of the position of profiles in the eddy. Both temperature and salinity decreased from the edge of the eddy (red profiles, highest dynamic height), toward the center (green profiles, above 900 dbar). Below 900 dbar, the center of the eddy was saltier but still colder than the surrounding waters.

The difference between the eddy properties at its center and the properties in the SAF near where the eddy was formed (Figure 5, dark blue, lowest dynamic height) indicated substantial change in water mass

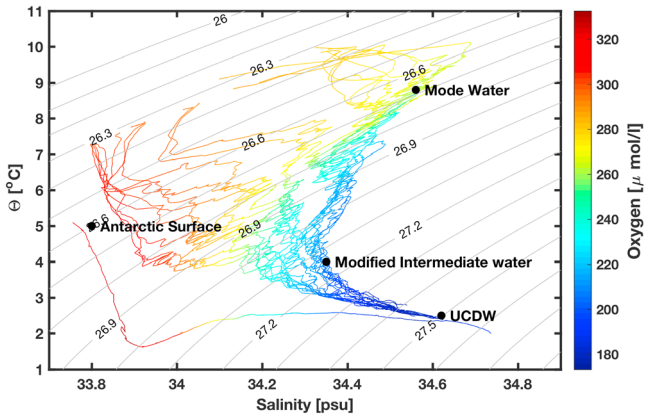

Figure 6. Θ-S diagram for all the conductivity-temperature-depth casts in Table 1, colored by dissolved oxygen. Different types of water observed in the Southern Ocean south of Tasmania are labeled (Rintoul & Bullister, 1999; Rintoul & Sokolov, 2001). UCDW = Upper Circumpolar Deep Water.

properties over the eddy's life span. The eddy's center was warmer than in the SAF at all depths, although the temperature difference varied with depth. The eddy center was slightly saltier than the SAF water above 200 dbar and fresher below (Figure 5). The convergence of all profiles near 1,500 dbar is an indication of the presence of Upper Circumpolar Deep Water (UCDW, oxygen minimum layer [175–180 μmol/L]), identified as salinity near 34.7 and density near 27.6 kg/m^3 (Figure 6). Note the high-frequency vertical variability below 100 dbar in salinity and temperature profiles, suggestive of active stirring on isopycnals in the eddy (Figure 5), which will be examined in a subsequent manuscript.

Water mass properties of temperature, salinity, and dissolved oxygen (Figure 6) suggested the core of the eddy was formed from Antarctic Surface Water above Antarctic Intermediate Water and UCDW. Subantarctic Mode Water (SAMW) was not present in the core of the eddy but encroached from the sides of the eddy between 100 and 800 dbar. This structure was consistent with the eddy having been formed south of the SAMW subduction region and moving northward into the SAZ where new ventilation by SAMW occurred.

Full-diameter hydrographic sections of temperature, salinity, and potential density distribution are presented in Figure 7. The sections revealed strong doming of isotherms and isopycnals as expected for a cold-core eddy. The surface mixed layer extended to approximately 100 dbar, and potential density of 26.6 kg/m^3, with horizontal gradients of warmer and saltier water at the edge of the eddy to cooler and fresher at the center. The doming of isopycnals extended from below the mixed layer to the limit of observations at 1,500 dbar. The extent of the isopycnal displacement is indicated by the 5 ° C isotherm, which was found at 150 dbar at the center of the eddy, 650 dbar shallower than its expected pressure in the SAZ (Rintoul et al., 2001). The salinity structure was more complicated. Isohalines domed upward to around 800 dbar beneath a bowl of relatively fresh water. The low salinity bowl (<34.4 g/kg) at the center was encroached upon by the 34.5-g/kg isohaline between 100 and 900 dbar (Figure 7, middle).

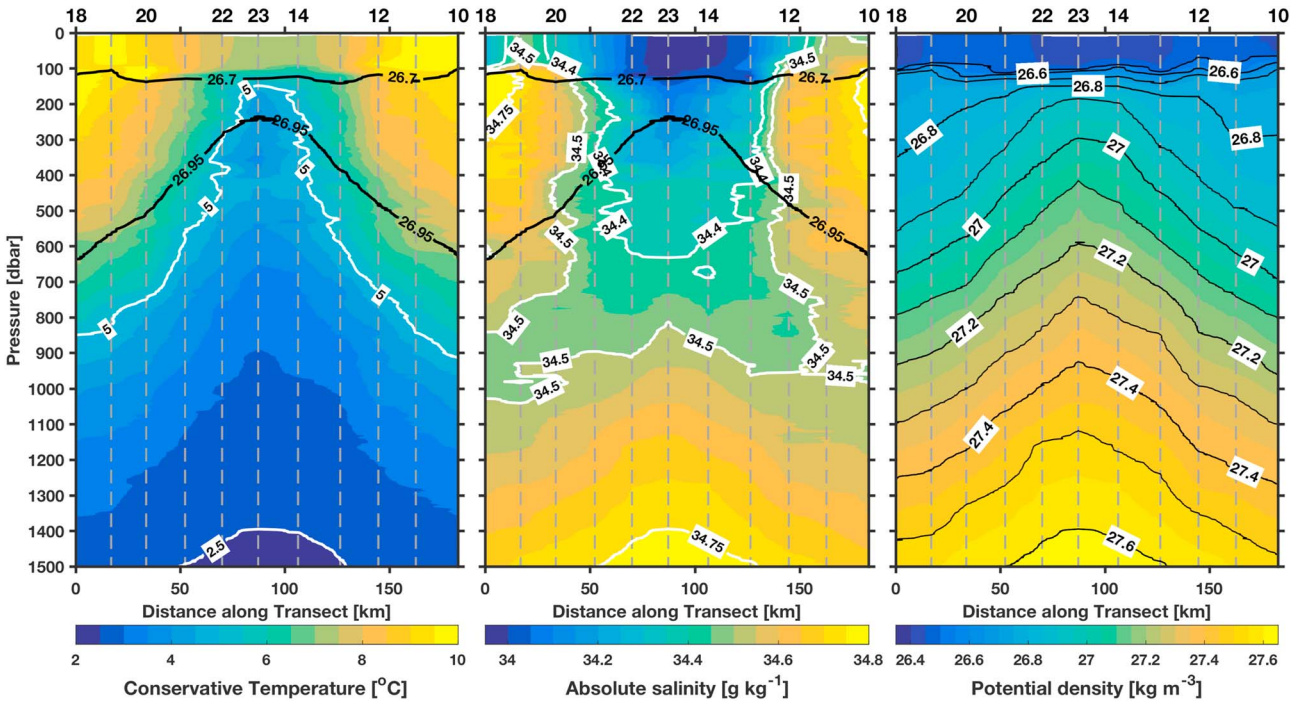

Figure 7. Vertical distribution of conservative temperature (left), absolute salinity (middle), and potential density (right). Black contours show potential density contours. This transect across the eddy was generated by merging conductivity-temperature-depth (CTD) transects B and C (for location, see Figure 1). Vertical dashed lines show CTD station positions. Top *x* axis represents CTD cast number.

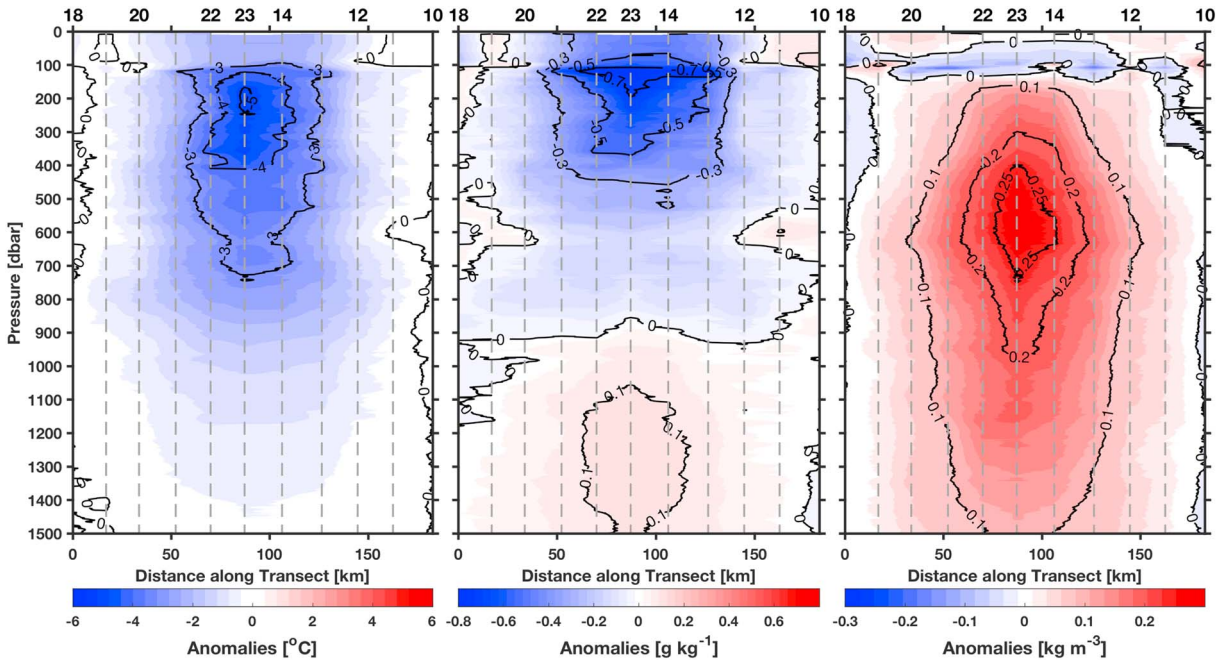

Figure 8. Vertical section of anomalies of conservative temperature (left), absolute salinity (middle), and potential density (right) on pressure levels relative to the reference profile representing ambient Subantarctic Zone water. Vertical dashed lines indicate conductivity-temperature-depth stations. Top *x* axis indicates conductivity-temperature-depth cast numbers.

Sections of property anomalies were constructed by subtracting reference profiles defined in section 2.4 from temperature, salinity, and density (Figure 8) on pressure levels. The maximum temperature anomaly at the eddy center was more than 5 ° C colder than the SAZ reference profile at a depth of 210 dbar (Figure 8, left). The temperature anomaly decreased monotonically to close to 0 at 1,500 dbar. A temperature minimum was evident in the mixed layer at the center of the eddy, but its magnitude was only 2 ° C, much smaller than deeper anomalies.

The maximum salinity anomaly was fresher than the reference profile by more than 0.7 g/kg at a depth of 100 dbar, right at the base of the mixed layer (Figure 8, middle). The salinity anomaly decreased monotonically with depth and changed sign near 900 dbar, suggesting a dipolar salinity structure in isobaric coordinates. A weaker salty anomaly of 0.1 g/kg was centered at 1,300 dbar. In the mixed layer, the salinity at the core of the eddy was still 0.4 g/kg fresher than at the edge, suggesting that the salinity signature of the eddy was not eroded as fast as its temperature signature, as has been reported in previous studies (Morrow et al., 2004).

The potential density anomaly (Figure 8, right) was positive from 150 dbar, just below the mixed layer, identifying the location and intensity of isopycnal doming throughout the water column. The maximum anomaly of 0.3 kg/m^3 was centered at 600 dbar. At the maximum depth of the observations the density anomaly in the eddy center was still more than 0.1 kg/m^3. A negative density anomaly dominated the mixed layer, indicating the influence of the salinity minimum on the stratification.

We prepared sections of property anomalies, computed on potential density surfaces, to identify the vertical extent of the eddy trapped water as presented in Figure 9. The main advantage of density as vertical coordinate is that it isolates the horizontal variation of water masses due to movement of density surfaces associated with available potential energy of the eddy (Joyce et al., 1981). The temperature anomalies increased rapidly from around 1 ° C in the mixed layer to a maximum value of 4 ° C in the core at 26.75 isopycnal and then gradually decreased to almost 0 at 1,500 dbar. Similarly, the salinity anomalies increased rapidly from 0.5 g/kg in the mixed layer to a maximum value of 0.75 g/kg in the core near 26.7 isopycnal and then gradually declined to <0.05 g/kg at 1,500 dbar. The distribution of anomalies indicates that our observations captured the full horizontal extent of the eddy, whereas the deepest part of the eddy was not captured by our survey. However, the magnitude of both anomalies at 1,500 dbar is only 5–10% of the maximum anomaly near 26.7 isopycnal and so will lead to only a small underestimate of the heat and salt

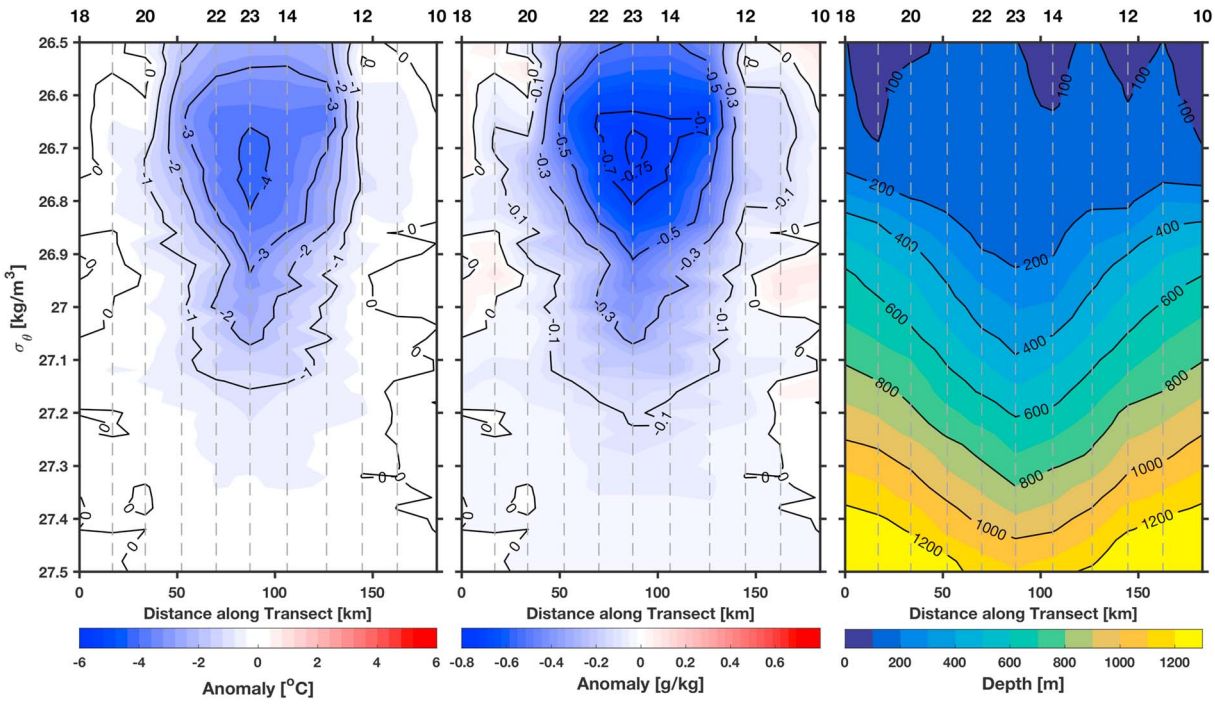

Figure 9. Vertical section of anomalies of conservative temperature (left) and absolute salinity (middle) on potential density surfaces relative to the reference profile representing ambient Subantarctic Zone water. The depth of isopycnals is shown in the right panel. The anomalies were calculated along the isopycnals. Vertical dashed lines indicate conductivity-temperature-depth stations. Top *x* axis indicates conductivity-temperature-depth cast numbers.

anomalies of the eddy. The eddy was fresher than ambient water over its entire density range, which is in contrast to the dipolar structure observed in the pressure coordinate (see Figure 8). The maximum temperature anomaly was 1 ° C lower than the anomaly on pressure surfaces in the core of the eddy whereas the maximum salinity anomaly was the same on the both coordinate systems in the core of the eddy.

3.3. Velocity Distribution

Cyclonic rotation and asymmetry of the eddy were evident in the geostrophic velocity from both altimetry and hydrography (Figure 10). The clockwise absolute geostrophic velocities were influenced by a jet coming from the northwest and merging with the northern side of the eddy (Figure 10, top). This may have been the cause of higher velocities on the eastern side and lower velocity on the western side of the center.

Subsurface geostrophic velocity was estimated from geopotential anomaly relative to a reference pressure of 1,500 dbar. Maximum velocities of >40 cm/s were observed above ~300 dbar on either side of the quiescent center (Figure 10, bottom) and decreased to 5 cm/s by ~1,300 dbar. Strong velocities of (>20 cm/s) extended from the surface down to 700 dbar on the northwestern side and to 850 dbar on the eastern side of the eddy. Maximum velocity was centered below the surface on both sides of the eddy, approximately 100 dbar on the northwestern side and 200 dbar on the eastern side. The absolute geostrophic velocity at the surface (Figure 10, top) also indicated stronger velocities on the eastern side.

In Figure 11, absolute velocities from the SADCP are plotted as vectors at 40 and 500 m and as vertical sections of tangential and radial components. Current vectors substantiate the presence of the mesoscale cyclonic feature and horseshoe shape (stronger current speed on eastern and southern sides) at both depths (Figure 11, top). The change in direction of vectors with depth, especially along the zonal transect (Figure 11, top; highlighted in red) indicated tilting of the eddy's vertical axis.

The positive tangential velocities on either side of the center indicated clockwise (cyclonic) rotation of the water column down to the limit of observations near 750 m, with velocities of >40 cm/s above 300 m on the western side and velocities >50 cm/s extending to 450 m on the eastern side. Tangential velocity maxima were found near 200 m on the western side and near 400 m on the eastern side, slightly deeper than that of the geostrophic velocities (Figure 10). There was also a surface velocity maximum of >60 cm/s on the eastern side of the eddy that was not apparent in the geostrophic velocity from CTD data.

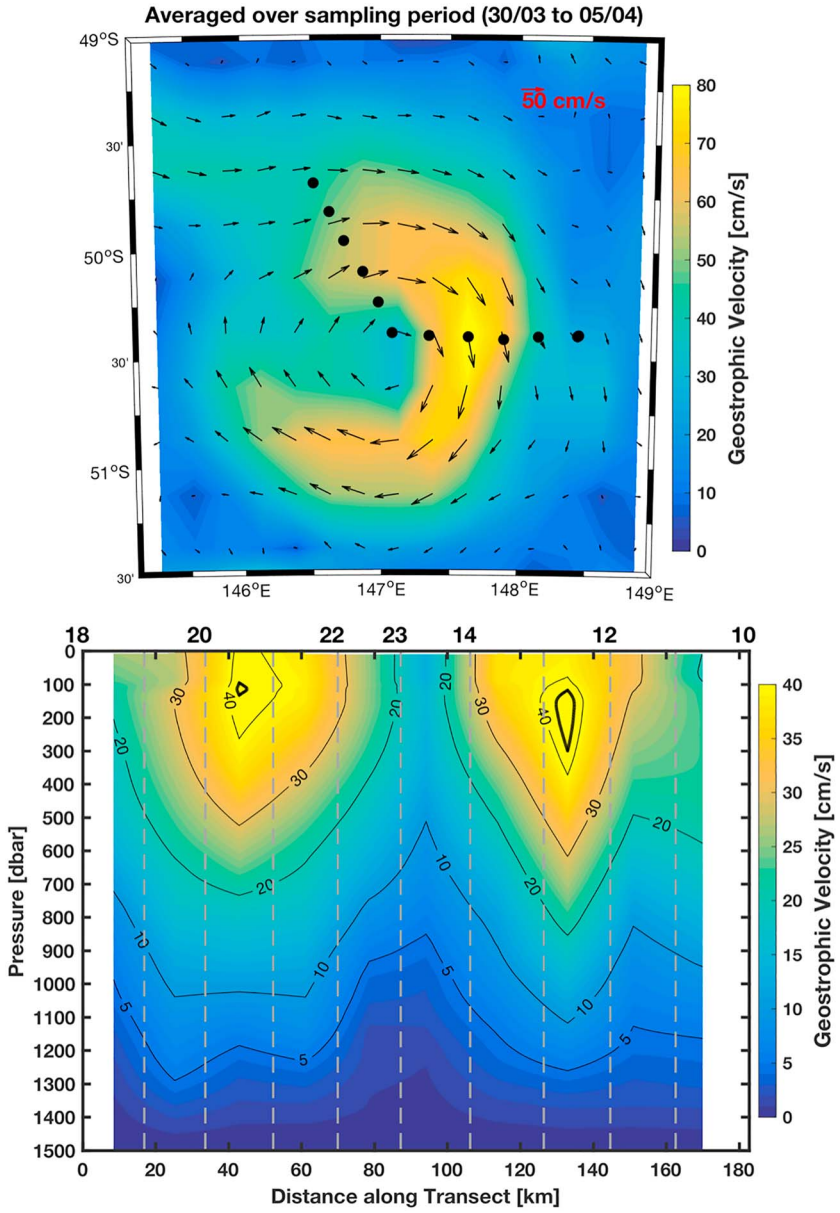

Figure 10. Geostrophic velocity distribution associated with the eddy. Horizontal distribution of absolute geostrophic velocity derived from absolute dynamic topography averaged over sampling period (top). Vertical distribution of geostrophic velocity with respect to 1,500 dbar (bottom) computed between each conductivity-temperature-depth station (location of casts shown as dashed lines in bottom panel and black dots in top panel). Positive geostrophic velocity indicates clockwise rotation (see text for detail). Top *x*-axis labels are conductivity-temperature-depth cast number. Thick black contours represent maximum velocities of 42 cm/s.

Radial velocities (Figure 11, bottom) were negative on the western side of the eddy, indicating flow toward the center, and positive on the eastern side, indicating flow away from the center. This pattern corroborates the hypothesis of an eastward-flowing filament of the ACC, seen with altimetry (Figure 10), interacting with the eddy to create asymmetry in the eddy's velocity field, weaker to the west and stronger to the east.

The magnitude of the absolute surface geostrophic velocities from altimetry were higher than the geostrophic velocities estimated from hydrography. This difference suggested that the unknown reference velocity at 1,500 dbar in the geostrophic calculation was of the order of 7 cm/s on the western side and 20 cm/s on the eastern side. Thus, all available velocity measurements concur on the strong cyclonic nature of the eddy's circulation and asymmetric distribution of velocity both horizontally and vertically.

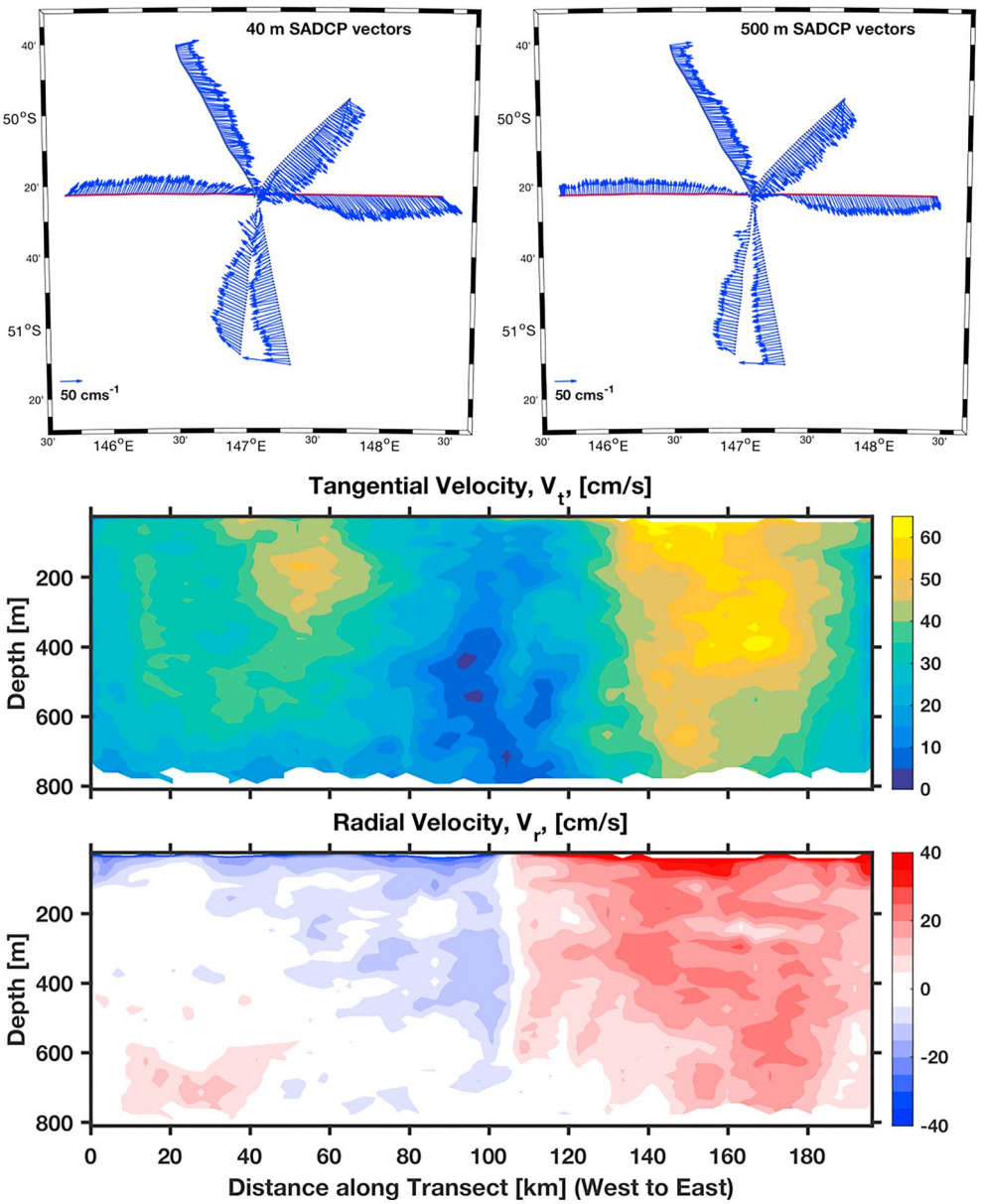

Figure 11. Velocity distribution from SADCP associated with the eddy. Horizontal velocity distribution at depth 40 and 500 m (top) and vertical velocity distribution of tangential (middle) and radial velocity (bottom) along west to east transect (highlighted in red, top panel) associated with the eddy. Positive tangential velocity indicates clockwise rotation, and positive radial velocity indicates outward flow. SADCP = shipboard acoustic Doppler current profiler.

3.4. Available Heat and Salt Anomalies

The AHA and ASA computations were performed for the composite CTD transect, and the resulting vertical distributions in isopycnal coordinates are presented in Figure 12 (top panels). They show a well-resolved structure, capturing almost to the full vertical extent of the eddy in terms of the salt anomaly and the vast majority of the vertical extent for the heat anomaly.

Heat content decreased rapidly with increasing density from -100×10^6 J/m^2 in the mixed layer to a maximum value of approximately $>-1,200 \times 10^6$ J/m^2 in the core at 26.95 kg/m^3. Salt content anomalies increased from a weak negative anomaly to a maximum value of approximately -50 kg/m^2 at 26.95 kg/m^3. Positive anomalies of the heat and salt were found near either edge of the eddy. It appears that the negative heat and salt content anomaly extended below the deepest isopycnal 27.45 kg/m^3. Therefore, our estimates of heat and salt content of the eddy will be conservative.

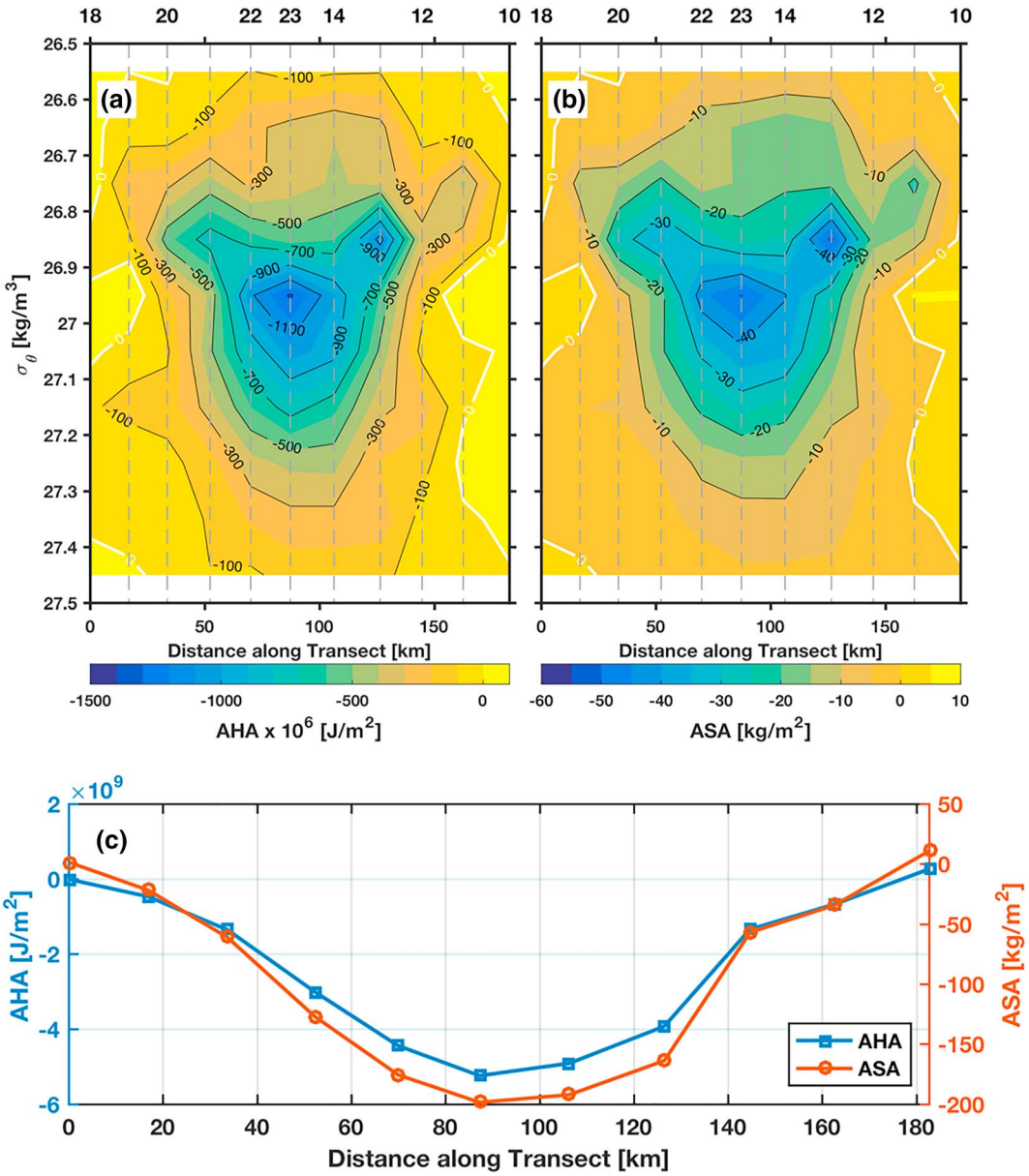

Figure 12. Distribution of available heat anomalies (a, AHA) and available salt anomalies (b, ASA) associated with the eddy with potential density as the vertical axis. Vertical dashed-lines indicate conductivity-temperature-depth stations. (c) Vertically summed AHA (left axis) and ASA (right axis) for given conductivity-temperature-depth stations, along the full-diameter transect. AHA = available heat content anomaly; ASA = available salt content anomaly.

The AHA and ASA were next summed vertically from densities of 26.5 to 27.5 kg/m^3 to give the heat and salt anomalies of the eddy as a function of eddy diameter, ΣAHA and ΣASA (Figure 12, bottom). The magnitude of the heat and salt anomalies increased from the edge of the eddy toward the center. The maximum negative heat and salt anomalies are -5×10^9 J/m^2 and -200 kg/m^2, respectively, at the center of the eddy.

Using equation (3), we integrated from the center of the eddy along each of the three radial transects to get three estimates of the total heat and salt anomalies associated with the eddy. Transects A and B are arranged from the center to the eastern edge, and transect C is arranged from the center to the northwestern edge. These estimates are presented in the Table 2. The eddy carried total available heat and salt anomalies of $\mathcal{H} = -0.5 \pm 0.1 \times 10^{20}$ J and $\mathcal{S} = -2.1 \pm 0.4 \times 10^{12}$ kg, respectively, computed as a mean of three transects and the standard error of the mean ($\sigma_M = \sigma/\sqrt{N}$, where σ is standard deviation and N is sample size). The standard error encapsulates the error associated with sampling the eddy in the presence of temporal variations during

Table 2
Total AHA and ASA Associated with the Eddy Calculated from Various CTD Transects using Equation (4)

Transect	$\mathcal{H}$ (J)	$\mathcal{S}$ (kg)
A	-0.67×10^{20}	-2.8×10^{12}
B	-0.47×10^{20}	-2×10^{12}
C	-0.34×10^{20}	-1.5×10^{12}
Mean	-0.5×10^{20}	-2.1×10^{12}
Standard Deviation (σ)	-0.17×10^{20}	-0.65×10^{12}

sampling and the nonsymmetrical spatial structure of the eddy. Despite sampling at the same locations on transects A and B, we sampled different parts of the eddy due to the eddy-structure rotation. We plotted vertically integrated contents along the distance from the center, for each radial transects (see Figure 14). The difference in contents between the transects were marginal for the stations close to the center and the edge of the eddy, whereas that of pronounced for the middle stations. This difference can be attributed to the variation of rotational speed along the eddy radius. The rotational speed increased from the center to a maximum value at midradius and then declined to the edge, forming a bell shape.

We conducted some sensitivity tests to determine the robustness of our estimates of total available heat and salt content anomalies, $\mathcal{H}$ and $\mathcal{S}$. A primary source of error in our estimate of $\mathcal{H}$ and $\mathcal{S}$ is the choice of reference profile. Our voyage was conducted during March/April when the SAZ is at its warmest and saltiest, which could lead to an overestimate of the heat and salt content of the cool, fresh eddy. To test the sensitivity of our heat and salt content anomalies to the reference profile, we recalculated them using a climatological mean profile and monthly climatological profiles for March and April from the gridded Argo atlas of Roemmich and Gilson (2009). We drew profiles from the climatology at the same positions, where the three in situ profiles were made, and averaged them. We found that while the upper 500 m of the in situ reference profile was warmer and saltier than all climatological profiles, the subsurface waters during the voyage were colder and fresher than seen in the climatology (figure not shown). The resulting total available heat and salt content anomalies were smaller using the annual mean climatological profile than the in situ profile by 13% and 16%, respectively, and were 6% and 3% larger, respectively, when the March or April climatological profiles were used. The in situ reference profile contained much greater vertical structure that was also present in the profiles inside the eddy and was representative of the SAZ conditions at the time of our observations. We are therefore confident that the in situ profile is the most appropriate, but note the 5–15% sensitivity of $\mathcal{H}$ and $\mathcal{S}$ to the choice of reference profile.

Note that we have used conservative temperature and absolute salinity to calculate heat and salt content anomalies. We find that the heat anomaly computed from conservative temperature was 0.6% lower than that from in situ temperature with varying heat capacity as calculated by Morrow et al. (2004). The salt anomaly calculated from absolute salinity was 0.5% higher than that computed from practical salinity.

3.5. An Altimetric View of the Eddy Population

To assess the dynamical properties of the eddy in comparison to other eddies of our region, delimited by 45–55° S and 135–155° E, we prepared a census of eddies over the 22-year period (1993 to 2014) using Faghmous et al. (2015) eddy diagnostics and eddy-tracking software. We tracked 1,025 cold-core (cyclones) and 957 warm-core (anticyclones) with life span greater than 30 days. We subsampled the cold-core eddies to find those that lived longer than 90 days to compare directly with our eddy properties. This filtering yielded 215 long-lived cyclones and 131 long-lived anticyclones that are formed in the region, regardless of their formation mechanism. While there was some interannual variability in the number of eddies found in the region, there was no detectable long-term trend. Since our census region was chosen to investigate cold-core eddies, it is not optimal for warm-core eddies, many of which are generated by poleward warm meanders further south. This may explain why fewer anticyclones were found.

From here on, we limit our investigation to cold-core eddies. These 215 eddies, comprising 32,385 realizations, had a median life span of 123 days. Their median amplitude, rotational speed, and equivalent diameter were 13.4 cm, 13.1 cm/s and 167.2 km, respectively. The rotational speed and amplitude of our eddy were larger than most eddies observed in the region. However, our eddy had a diameter and life span close to

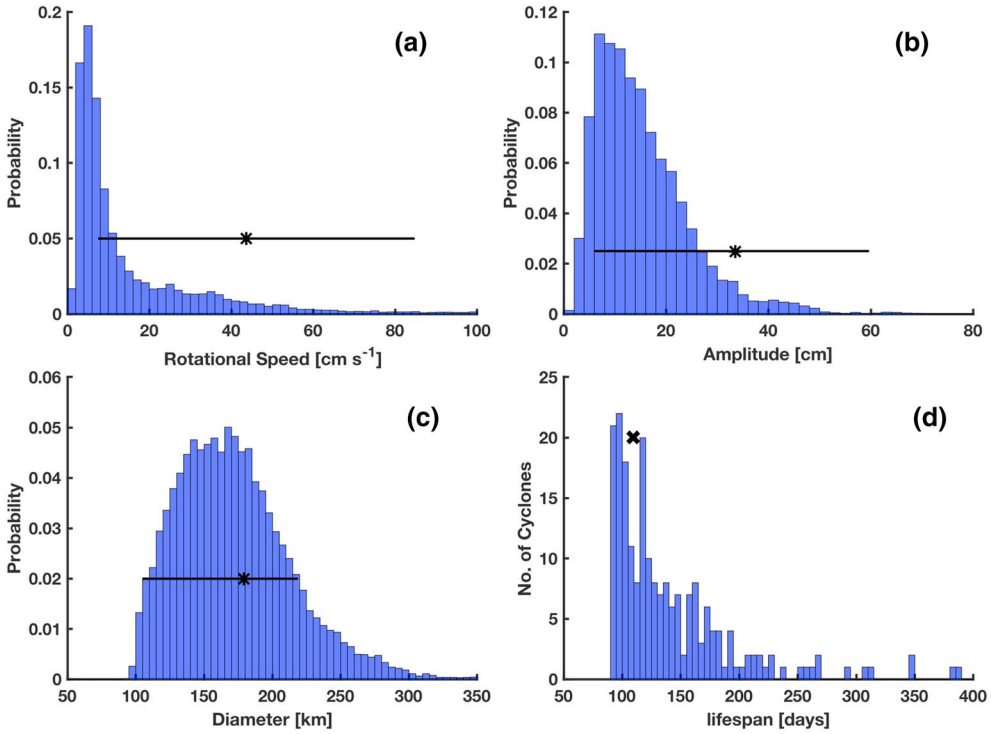

Figure 13. Histograms of rotational speed, diameter, amplitude, and life span of cyclonic eddies in our region of interest (45–55°S; 135–155°E) with a lifetime greater than 90 days. Here *Y* axis represents the probability of observation (number of observations in a bin/total number of observations) for rotational speed, diameter and amplitude. In (a)–(c), the horizontal line shows the range observed for our eddy over its lifetime; the asterisk is the median for our eddy. In (d), the *Y* axis is number of cyclones with a given life span. The cross mark in (d) depicts the life span of our eddy.

the median of the population (see Figure 13). We also constructed histograms for eddies observed in each season (December–February, March–May, June–August, and September–November) in the same way as for Figure 13 (not shown here). We observed no noticeable difference in the seasonal distribution of cyclonic eddies' characteristics. We concluded that our eddy was a typical long-lived eddy for our region in terms of diameter, but its amplitude and rotational speed were at the high end of the range compared with eddies in the census.

4. Discussion

4.1. Observed Structure of a Cyclonic ACC Eddy

We sampled a cold-core (cyclonic) eddy in the SAZ to examine its vertical structure. We observed eddy-induced uplifting of isopleths of temperature, salinity, and potential density that extended to the limit of observations at 1,500 dbar (Figure 7). This deep penetration of the cyclonic eddy is consistent with earlier studies. A 3-D eddy census revealed that south of Tasmania has the deepest eddies in the world (Petersen et al., 2013). Phillips and Rintoul (2000) found that the eddy signature for south of Tasmania extend to 3,000 m. Joyce et al. (1981) and Swart et al. (2008) reported that cold-eddy rings in the Drake Passage and south of Africa penetrate to at least 1,000 m based on field observation. Finally, a composite structure of SO eddies showed that they penetrate to at least 2,000 m (Frenger et al., 2015).

The eddy was cold throughout the water column with a maximum cold anomaly of more than 5 ° C near 200 dbar (Figure 8). The eddy's salinity had a dipolar vertical structure when viewed in pressure coordinates, with fresh anomalies from the surface to 900 dbar and a maximum fresh anomaly of >0.7 g/kg at the base of the mixed layer. A weaker salty anomaly of about 0.1 g/kg was observed near 1,300 dbar, indicating the presence of UCDW at shallower levels inside the eddy than found in the undisturbed SAZ. The temperature and salinity anomalies resulted in a negative potential density anomaly that was less dense than surrounding waters in the mixed layer and more dense from the base of the mixed layer to 1,500 dbar. The maximum density anomaly was more than 0.25 kg/m^3 centered at 600 dbar.

Table 3
Selected Previous Estimate of Available Heat and Salt Anomalies for the Antarctic Circumpolar Current's Cyclonic Eddies

Author	Region	Area (m^2)	Depth (dbar)	$\mathcal{H}$ (J)	S (kg)
Joyce et al. (1981)	Drake Passage	0.55×10^{10}	1,100	$\mathbf{-0.12 \times 10^{20}}$	$\mathbf{-0.25 \times 10^{12}}$
Swart et al. (2008)	South of Africa	1.64×10^{10}	1,000	-0.54×10^{20}	-0.66×10^{12}
Swart, depth adjusted	South of Africa	1.64×10^{10}	1,500	$\mathbf{-0.61 \times 10^{20}}$	$\mathbf{-0.75 \times 10^{12}}$
Morrow et al. (2004)	South of Tasmania	0.79×10^{10}	1,000	-0.19×10^{20}	-0.82×10^{12}
Morrow linear model	South of Tasmania	0.79×10^{10}	1,000	[a] -0.28×10^{20}	[a] -1.1×10^{12}
Morrow linear model, depth adjusted	South of Tasmania	0.79×10^{10}	1,500	[a] $\mathbf{-0.32 \times 10^{20}}$	[a] $\mathbf{-1.3 \times 10^{12}}$
This study	**South of Tasmania**	$\mathbf{1.67 \times 10^{10}}$	**1,500**	$\mathbf{-0.5 \times 10^{20}}$	$\mathbf{-2.1 \times 10^{12}}$

Note. Depth is an approximate depth at the eddy center. Bold figures highlight the values from other studies that may be directly compared with $\mathcal{H}$ and S from our study, having either been adjusted to account for incomplete sampling or were already complete, as in Joyce et al. (1981). See text for details of the linear model and depth adjustment.
[a]Scaled estimate based on linear regression model.

The water mass anomalies inside our eddy were similar to those found for cold eddies south of Africa (Swart et al., 2008), in Drake Passage (Joyce et al., 1981), and previously reported south of Tasmania (Morrow et al., 2004). Our observations are also consistent with the composite structure for cold eddies found north of the ACC as reported by Frenger et al. (2015). A strong mixed layer was present in the upper 100 dbar where lateral gradients across the eddy were more than 2 times weaker than below the mixed layer. The mixed layer capping had a substantial impact on biogeochemistry of the eddy (Moreau et al., 2017).

In our velocity observations, we observed that filaments of the ACC interacted with the eddy's velocity distribution, highlighting its asymmetric structure, and likely contributing to strong interleaving on isopycnals. In future work, we will quantify the isopycnal stirring and diapycnal mixing that could be responsible for the difference in the observed water mass properties of the eddy and properties in the SAF near where the eddy was formed.

4.2. Available Heat and Salt Anomalies

The eddy's total heat content anomaly, $\mathcal{H} = -0.5 \times 10^{20}$ J, and total salt content anomaly, $S = -2.1 \times 10^{12}$ kg, are either more intense than or equivalent to those previously reported for ACC cyclonic eddies (Table 3). In this section, we examined potential undersampling of the eddies in earlier studies, and where justified, scale up the earlier estimates of heat and salt content anomalies.

The observations of Joyce et al. (1981) captured the full vertical and horizontal structure of the PF eddy as shown in their Figure 16. However, their eddy only extended to 1,100 m, and its surface area was 3 times smaller than ours, limiting the size of the heat and salt anomalies it could carry. It is not clear if these differences in eddy size were due to the difference between eddies generated in the PF and SAF, regional difference between Drake Passage and south of Tasmania, or whether a smaller eddy was sampled in a population of eddies with characteristics similar to those in our region. We observed similar vertical distribution of AHA and ASA to Joyce et al.'s (1981) eddy; however, the core of their eddy had relatively lower heat and salt anomalies than ours (their Figure 16, our Figure 12). Cold and fresh anomalies in their eddy were concentrated in the density range of 27.2 to 27.5 kg/m^3, whereas our anomalies were concentrated at lighter levels from 26.6 to 27.3 kg/m^3.

The eddy of Swart et al. (2008) was sampled vertically to 1,000 m. However, in this case, the full vertical extent of the eddy was not captured, and they reported that their estimate of AHA was likely biased low. The diameter of their eddy was similar to ours, and their observations captured the full horizontal extent. To quantify the missing AHA due to incomplete vertical sampling of the Swart et al. (2008) eddy, we subsampled our eddy to 1,000 dbar, rather than the full 1,500 dbar. We find that it reduced the heat content magnitude to 88% of the full AHA. If we apply this factor to scale up Swart et al.'s (2008) 1,000 dbar to a 1,500-dbar estimate, we obtain -0.61×10^{20} J. For salt, the scaling factor is the same and the Swart et al. (2008) estimate scales up to -0.75×10^{12} kg. This implies the heat content for their eddy is 1.2 times higher than our eddy, and their salt content is still 2.8 times smaller. In comparison to our eddy's heat and salt content structure (Figure 12), their eddy had quite different structure; see their Figure 9. The core of their heat content anomaly was on a much denser isopycnal than that of salt content anomaly (27.7 vs. 27.4 kg/m^3). For our eddy, the heat and salt content anomaly cores were both centered on the isopycnal 26.95 kg/m^3. These results suggest that the

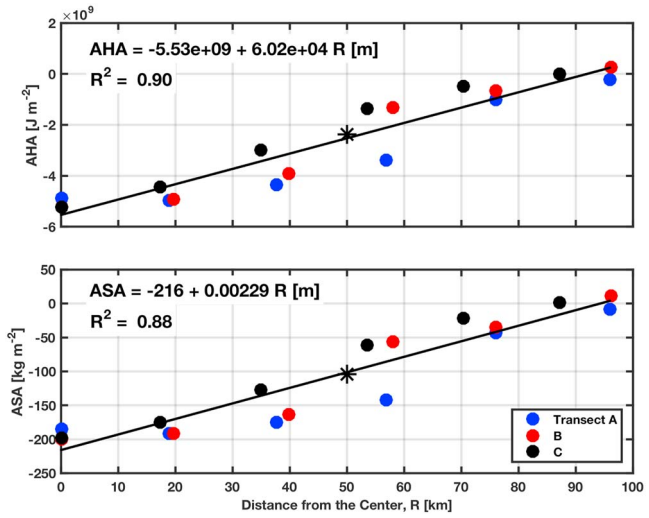

Figure 14. Linear regression model for available heat anomaly (top) and available salt anomaly (bottom) from all 18 conductivity-temperature-depth profiles sampled in the eddy. Morrow et al. (2004) values of total AHA and ASA are marked as asterisk. AHA = available heat content anomaly; ASA = available salt content anomaly.

difference between these two eddies is likely due to regional heterogeneity rather than eddy size and may be influenced by differences due to random sampling in both studies of an eddy population with a range of characteristics in the respective locations.

Morrow et al. (2004) reported the first estimate of total AHA and ASA south of Tasmania based on two CTD casts that glanced the edge of an eddy (see their Figure 10d, red contour, approximate location is shown in Figure 1, plus sign). Their CTDs were approximately 50 km from the center of the eddy and so did not sample the deep cold, fresh center of their eddy. For our eddy, the AHA and ASA at 50 km are only ~51% and ~ 57% of the value in the center, respectively. To quantify the underestimate, we developed a linear relationship between AHA/ASA and distance from the center (R) of our eddy as shown in Figure 14. We tested various curve-fitting techniques to reduce root-mean-square error and improve R^2 value of the fit to the heat and salt content. Owing to the marginal impact of different curve-fitting techniques on root-mean-square error and R^2 value, our linear-fit seemed appropriate for the estimation. We also plotted the ΣAHA and ΣASA reported by Morrow et al. (2004) in Figure 14. Their estimate of heat and salt at 50 km is in close agreement with our estimate, indicating that both eddies were likely to have similar contents. Using the linear relationship and equation (3), we computed the total heat and salt content anomalies for the Morrow et al. (2004) eddy that are of -0.28×10^{20} J and -1.1×10^{12} kg, respectively. If we then scale up their 1,000-dbar estimate to 1,500 dbar, as we did for the Swart et al. (2008) eddy, we find a total heat content for the Morrow et al. (2004) eddy of -0.32×10^{20} J and salt content of -1.3×10^{12} kg. These are 0.64 times smaller for heat and 0.62 times smaller for salt than found in our eddy in the same region.

Based on our scale adjustments to the results reported in earlier studies, we suggest that previously reported total heat and salt content anomalies of SAF eddies south of Tasmania were underestimated by a factor of 2.6 for heat and 2.5 for salt, owing to incomplete eddy sampling. Therefore, the total heat and salt content of a cold-core SAF eddy entering the SAZ is substantially more than previously reported. We next examine the impact of this on our understanding of the poleward transfer of heat and salt.

4.3. Poleward Fluxes of Heat and Salt

We combine the detailed in situ observations of our cold-core eddy with the eddy census from satellite altimetry. This approach assumes that a snapshot of one eddy at one time can be used to track the evolution of the eddy's heat and salt content over time, based on its surface characteristics of amplitude and diameter. It also assumes that this relation holds for all cold-core eddies formed over our 20° longitude region and that any variations in the eddy's vertical structure and heat/salt content are captured by this simple relation. All of the eddies that we are considering are generated from instabilities in the SAF that capture water from south of the SAF. Thus, the isopycnal tilt in each eddy and the properties of the core are likely to be similar in all of the eddies. Given the sparsity of observations, we believe the approach is justified as a means to obtain an in situ estimate of poleward fluxes that extends beyond our single snapshot observations. Nonetheless, the approach is supported by the fact that temperature and salinity characteristics (at any discrete depth or integrated across them) can be directly related to the SLA in the SO. The approach has been used to great advantage in the development of gravest empirical mode climatologies (Sun & Watts, 2001) and time-varying fields (Meijers et al., 2011; Swart et al., 2010).

We aim to quantify the impact of the historical population of eddies on the poleward flux of heat and salt through the cooling and freshening of the SAZ by cold-core SAF eddies in the longitude range 135–155° E. We first of all define a relationship between the subsurface heat and salt content of our eddy from the in situ observations and the surface expression of the eddy revealed by the tracking algorithm. The Integrated Surface Elevation (ISE) gives an approximation to the volume of the eddy that rises above the zero SLA contour. If we assume that the elevated surface of an eddy has a conical shape, then ISE can be calculated as 1/3 × Surface Area × Amplitude. The average amplitude and surface area of our eddy at the time of the sampling, based on the satellite SLA data and extracted by the tracking software, were 45.87 cm and

3.085×10^4 km^2, respectively, giving an ISE for the survey period of 4.72×10^9 m^3. The surface area parameter is readily obtained from the eddy-tracking software and is based on the number of pixels occupied by the eddy at a given time, and does not assume that the eddy is circular (Faghmous et al., 2015). If we assume a linear relationship between ISE and eddy heat and salt content as in Swart et al. (2008), we can determine a simple empirical relationship between the time-varying ISE of the cold-core eddy and its time-varying total heat and salt content anomaly, assuming that our eddy is typical. Thus, an empirical relationship between the total heat/salt content and ISE from our eddy is

$$\mathcal{H} = -1.06 \times 10^{10} \cdot ISE(\mathrm{J}); \mathcal{S} = -445 \cdot ISE(\mathrm{kg}). \quad (4)$$

We can then apply this relationship to estimate the amount of heat and salt delivered into the SAZ by the entire population of cold-core SAF eddies during the altimetry period based on their amplitude and surface area.

In section 3.5, we detected 215 cyclones in 22 years (1993–2014), 63 of which were long-lived (>90 days) eddies that could be identified as forming due to SAF instability. Among these eddies, 29 (46%) dissipated in the SAZ and 29 (46%) dissipated in the SAF, while the fate of 5 (8%) eddies was undecided because they left the study region.

We divided the 63 eddies into three categories based on their dissipation site and examined their life cycle through satellite animation. We observed that 46% of eddies detached from the SAF meander and never returned to the SAF losing their heat to the SAZ. From 46% of eddies that dissipated in the SAF, 15 eddies never left the SAF after they were formed and so contributed no heat at all into the SAZ and 14 eddies spent some amount of time in the SAZ before they were reabsorbed into the meander, thereby contributing a fraction of their heat anomaly to the SAZ. We calculated their heat contribution to the SAZ by subtracting their heat anomaly at dissipation from their maximum heat anomaly and similarly for salt anomaly.

The eddies that dissipated in the SAZ carried a total of -1.25×10^{21} J, while the eddies that dissipated in the SAF contributed of -0.7×10^{21} J to the SAZ. Therefore, the total heat transferred into the SAZ by all long-lived cold-core eddies over the 22-year period is -1.95×10^{21} J. On average, cold-core eddies contribute an annual heat anomaly of $-0.89 \pm 0.11 \times 10^{20}$ J into the SAZ, over the 20° longitude region.

Likewise, the eddies that dissipated in the SAZ transport a total salt anomaly of -5.25×10^{13} kg, while the eddies that dissipated in the SAF contributed of -2.94×10^{13} kg to the SAZ. Therefore, the total salt transferred into the SAZ by all long-lived cold-core eddies over the 22-year period is -8.19×10^{13} kg. Thus, on average, cold-core eddies contribute an annual salt anomaly of $-3.72 \pm 0.46 \times 10^{12}$ kg into the SAZ over this region.

The empirical relationship that we used to estimate total heat and salt content from ISE of eddies found in the altimeter record has errors from the in situ estimate of heat and salt content for our observed eddy and errors associated with the measurement of the amplitude and surface area of the eddy from altimetry. Rather than estimating errors associated with each of these and propagate them through the calculation, we take a simpler approach. Possibly the largest source of error in this calculation is in the eddy detection step. We have found the tracking algorithm to be very reliable when compared to a manual tracking method for individual eddies. However, we may overestimate or underestimate the number of eddies from one year to the next. We define an error bar for the total heat transport into SAZ by the long-lived cold-core SAF eddies in the altimeter record to be the standard error in the mean transport by eddies found in three overlapping 11-year periods (1993–2003, 1998–2008, and 2004–2014). As we did for the 22-year period, we identified the eddies that are formed at the SAF and deliver heat to the SAZ in each 11-year block, and we determined the annual heat transport in each 11-year block table 4. We calculate the standard error from the three estimates and use this as our error estimate for the total heat transport per year by long-lived cold-core eddies in our region. We do a similar calculation for salt transport. The result is an error bar of 0.11×10^{20} and 0.46×10^{12} for the total heat and salt transport into the SAZ, respectively.

The amount of heat carried by long-lived cold-core eddies south of Tasmania was compared with the Foppert et al. (2017) satellite-proxy-derived EHF for the same region (shown as a dashed box in Figure 1). We followed the Foppert et al. (2017) calculation to determine the time mean, depth integrated to 2,000 m, downgradient EHF over the same period as our eddy census (Figure 15). We used $EHF = A \cdot H^{*B}$, where H^* is the SSH standard deviation calculated for the period 1993–2014, where $A = -1.85 \pm 0.17 \times 10^4$ and

Table 4
Total Heat and Salt Anomaly Carried Into Subantarctic Zone by the Eddies That Dissipated in SAZ and SAF Over Three Overlapping 11-Year Periods, Estimated From Equation (4)

	Eddies		$\mathcal{H}$ (J)		$\mathcal{S}$ (kg)	
Period	SAZ	SAF	SAZ	SAF	SAZ	SAF
1993–2003	17	6	-6.95×10^{20}	-3.73×10^{20}	-2.92×10^{13}	-1.57×10^{13}
1998–2008	12	4	-4.68×10^{20}	-1.85×10^{20}	-1.96×10^{13}	-0.78×10^{13}
2004–2014	12	8	-5.52×10^{20}	-3.29×10^{20}	-2.32×10^{13}	-1.38×10^{13}
Annual standard error of mean			0.11×10^{20}		0.46×10^{12}	

Note. SAF = Subantarctic Front; SAZ = Subantarctic Zone.

$B = 3.95 \pm 0.12$ are the best fit power law coefficients as reported by Foppert et al. (2017). Also shown in Figure 15 are the trajectories of the 63 long-lived SAF eddies captured in our census. We find an average EHF over our region of -2.95×10^{14} J/m/year (converted from −9.35 MW/m). If we multiply by the zonal distance of the 20° box (1.4×10^6 m), we obtain an annual flux of -4.13×10^{20} J. Our estimate of the annual heat transport into the SAZ by all cold-core eddies in the same region is -0.89×10^{20} J. We conclude that the annual poleward heat flux due to long-lived cold-core eddies moving into the SAZ between 135° E and 155° E is 21.5% of the total poleward heat flux by all heat transfer mechanisms across this 20° longitude band. The other possible mechanisms include warm-core eddies moving into the PF Zone, short-lived eddies of both sign, and smaller-scale processes that are not resolved by the altimeter. It is possible that some of these small-scale processes could counteract the poleward flux of heat by the long-lived eddies through restratification of the water column. The hotspot of EHF to the south of the SAF between 148° E and 153° E where a large poleward meander exists is likely to be the domain of warm-core eddies fluxing heat poleward. So, while the cold-core eddies appear to be responsible for approximately 21% of the poleward heat flux, they do this more uniformly across the domain than warm-core eddies, which appears to be more intense and very localized.

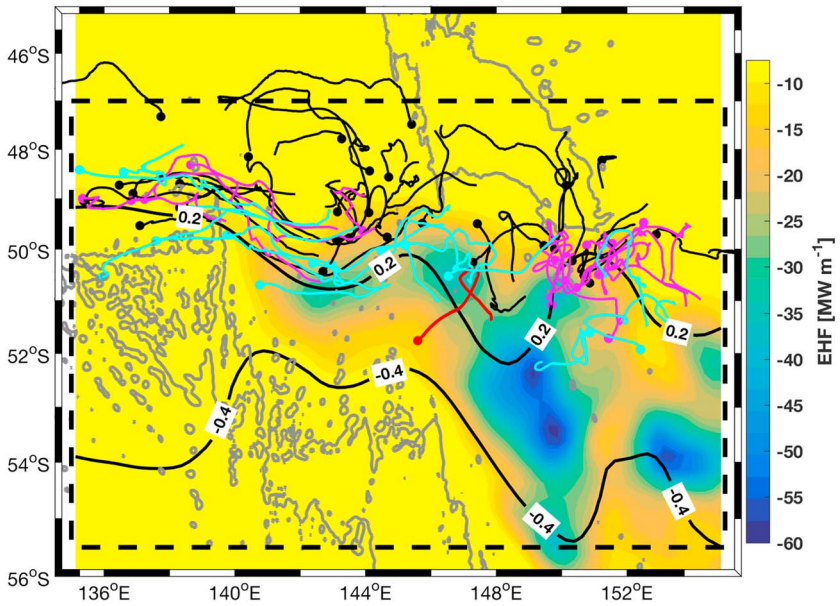

Figure 15. Poleward eddy heat flux calculated following Foppert et al. (2017) (shading). Trajectories of 63 long-lived cold-core eddies formed at the Subantarctic Front (SAF) between 1993 and 2014. First recorded position is marked by a dot. Three categories of eddies are shown: eddies that are dissipated in the Subantarctic Zone (SAZ; black), eddies that enter the SAZ but return to the SAF prior to dissipating (magenta), and eddies that never leave the SAF (cyan). Black contours show climatological positions of the northern and southern branches of the SAF estimated over the 22-year period (1993–2014), based on absolute dynamic topography of 0.2 and −0.4 m, respectively (Sokolov & Rintoul, 2009). EHF = eddy heat flux.

We also estimate the impact of cold-core eddies on the freshwater budget of the SAZ in the same manner as Morrow et al. (2004). We consider the fresh capping by Ekman transport into the SAZ to be a 50-m-deep layer holding a salinity anomaly of −0.6 g/kg, extending 50 km north of the SAF and extending 20° zonally (1.4×10^6 m). This amounts to a total salt anomaly of -2.2×10^{12} kg due to Ekman transport. The annual salt anomaly calculated from our eddy census is -3.72×10^{12}, which is about 1.7 times that carried by Ekman transport. As such, we believe that long-lived cold-core eddies are as important as the Ekman freshwater flux in controlling the freshwater budget of the SAZ.

Hogg et al. (2015) find a decadal increase in eddy kinetic energy since the early 1990s that has occurred in conjunction with the increasing trend in the Southern Annular Mode in recent decades. While we found no evident interannual trend in the number of eddies in our census region, increased eddy kinetic energy across the ACC could be carried by more intense eddies, with a corresponding increase in poleward eddy heat and salt fluxes. This will likely have important consequences to the water mass properties of the northward branch of the shallow overturning circulation via SAMW and potentially to the uptake of heat and carbon dioxide in the SAZ.

5. Conclusion

Mesoscale eddies are ubiquitous in the SO and play a critical role in the poleward transport of heat and salt. Our study provides new insights into the role played by cold-core SAF eddies in this transport by characterizing the three-dimensional structure of a cold-core eddy, based on field observations south of Tasmania. Our results show that the heat and salt anomalies carried by this type of eddies have been previously underestimated by a factor of approximately 2.6 for heat and 2.5 for salt, largely due to incomplete eddy sampling in south of Tasmania. We propose that these eddies contribute approximately 21% of the total poleward EHF across the SAF, with the remainder being contributed by short-lived cold core eddies, warm-core eddies, and smaller scales. The annual freshwater flux into the SAZ by long-lived cold-core eddies is of the same order of magnitude as the Ekman freshwater flux in this region. Increased eddy activity as projected for the future could have a substantial impact on the heat and salt budgets of the SAZ and consequently on the uptake of heat and carbon dioxide into the SO.

Acknowledgments
This research was supported by an Australian Research Council Discovery Project (DP160102870), the Australian Research Council's Special Research Initiative for Antarctic Gateway Partnership (SR140300001), and ship time from Australia's Marine National Facility. We thank the officers, crew, and technical staff of Australia's Marine National Facility R.V. Investigator for their help with data collection. We are also grateful to our shipmates from the Eddy, CAPRICORN, and SOTS projects. We thank AVISO and CMEMS for providing near-real-time altimetry data. We are thankful to Faghmous et al. (2015) for disseminating eddy-tracking software and their diagnostic. We thank R. Pawlowicz for m_map mapping Matlab Toolbox (www.eos.ubc.ca/∼rich) and Trevor McDougall and Paul Barker for Gibbs-SeaWater Oceanographic Matlab Toolbox (GSW v3.05). R. P. thanks Benoit Legresy for AVISO products. R. P. thanks QMS PhD program for providing financial support to conduct his research. R. P. also acknowledges Gabriela S. Pilo's input in setting up the manual eddy-tracking software. H. P. acknowledges funding from the Australian Government's National Environmental Science Program. This study is part of the EDDY project: http://southernoceaneddie.wixsite.com/eddies. R. P. and H. P. thank Prof. Nathan Bindoff for valuable comments on uncertainty estimates. Comments from four anonymous reviewers greatly improved this manuscript.

Appendix A: Amendment to Faghmous Tracking Algorithm

The eddy-tracking software is based on a geometric definition such that every eddy must have a single extremum inside a closed contour of SLA. The extremum is defined by comparing each grid point with its neighboring grid points. Once extrema are defined, the software searches for closed contours surrounding those extrema to exclude noneddy features, such as frontal meanders. The software tracks eddies through time following the Chelton et al. (2011) method with an additional feature that allows an eddy to disappear for some user-defined period, depending on the temporal resolution of data.

We adapted the tracking algorithm of Faghmous et al. (2015) to better suit the tracking of eddies within a small region. This was necessary to obtain correct diameter of eddies. The surface area estimation algorithm of Faghmous et al. (2015) generated erroneous "area map.mat" file, and therefore spurious diameter of eddies, while applied for our regional study. We modified the surface area estimation algorithm by making it dependent on given latitudes and longitudes. Therefore, the new algorithm is best suited for both regional- and global-scale studies.

We have rewritten a script (set_up_ssh_data.m) for the regional application of Faghmous et al. (2015) software to preprocess SLA data, renamed to set_up_data_regional.m . Further detail pertaining to the script is given in the technical document. The technical document and scripts are available from authors.

References

Chelton, D. B., Schlax, M. G., & Samelson, R. M. (2011). Global observations of nonlinear mesoscale eddies. *Progress in Oceanography*, *91*(2), 167–216.

Chelton, D. B., Schlax, M. G., Samelson, R. M., & de Szoeke, R. A. (2007). Global observations of large oceanic eddies. *Geophysical Research Letters*, *34*, L15606. https://doi.org/10.1029/2007GL030812

de Boyer Montégut, C., Madec, G., Fischer, A. S., Lazar, A., & Iudicone, D. (2004). Mixed layer depth over the global ocean: An examination of profile data and a profile-based climatology. *Journal of Geophysical Research*, *109*, C12003. https://doi.org/10.1029/2004JC002378

de Szoeke, R. A., & Levine, M. D. (1981). The advective flux of heat by mean geostrophic motions in the Southern Ocean. *Deep Sea Research Part A. Oceanographic Research Papers*, *28*(10), 1057–1085.
Dufour, C. O., Griffies, S. M., de Souza, G. F., Frenger, I., Morrison, A. K., Palter, J. B., et al. (2015). Role of mesoscale eddies in cross-frontal transport of heat and biogeochemical tracers in the Southern Ocean. *Journal of Physical Oceanography*, *45*(12), 3057–3081.
Faghmous, J. H., Frenger, I., Yao, Y., Warmka, R., Lindell, A., & Kumar, V. (2015). A daily global mesoscale ocean eddy dataset from satellite altimetry. *Scientific Data*, *2*, 150028.
Faghmous, J. H., Nguyen, H., Le, M., & Kumar, V. (2014). Spatio-temporal consistency as a means to identify unlabeled objects in a continuous data field. In *AAAI'14 Proceedings of the Twenty-Eighth AAAI Conference on Artificial Intelligence*, pp. 410–416.
Ferrari, R., Provost, C., Park, Y.-H., Sennéchael, N., Koenig, Z., Sekma, H., et al. (2014). Heat fluxes across the Antarctic Circumpolar Current in Drake Passage: Mean flow and eddy contributions. *Journal of Geophysical Research: Oceans*, *119*, 6381–6402. https://doi.org/10.1002/2014JC010201
Foppert, A., Donohue, K. A., Watts, D. R., & Tracey, K. L. (2017). Eddy heat flux across the Antarctic Circumpolar Current estimated from sea surface height standard deviation. *Journal of Geophysical Research: Oceans*, *122*, 6947–6964. https://doi.org/10.1002/2017JC012837
Frenger, I., Muennich, M., Gruber, N., & Knutti, R. (2015). Southern Ocean eddy phenomenology. *Journal of Geophysical Research: Oceans*, *120*, 7413–7449. https://doi.org/10.1002/2015JC011047
Hogg, A. M., Meredith, M. P., Chambers, D. P., Abrahamsen, E. P., Hughes, C. W., & Morrison, A. K. (2015). Recent trends in the Southern Ocean eddy field. *Journal of Geophysical Research: Oceans*, *120*, 257–267. https://doi.org/10.1002/2014JC010470
Intergovernmental Oceanographic Commission (2010). The international thermodynamic equation of seawater–2010: Calculation and use of thermodynamic properties.[includes corrections up to 31st october 2015].
Johnson, G. C., & Bryden, H. L. (1989). On the size of the Antarctic Circumpolar Current. *Deep Sea Research Part A. Oceanographic Research Papers*, *36*(1), 39–53.
Joyce, T., Patterson, S., & Millard, R. (1981). Anatomy of a cyclonic ring in the Drake Passage. *Deep Sea Research Part A. Oceanographic Research Papers*, *28*(11), 1265–1287.
Keffer, T., & Holloway, G. (1988). Estimating Southern Ocean eddy flux of heat and salt from satellite altimetry. *Nature*, *332*(6165), 624–626.
Kurczyn, J. A., Beier, E., Lavin, M. F., Chaigneau, A., & Godinez, V. M. (2013). Anatomy and evolution of a cyclonic mesoscale eddy observed in the northeastern Pacific tropical-subtropical transition zone. *Journal of Geophysical Research: Oceans*, *118*, 5931–5950. https://doi.org/10.1002/2013JC20437
Lumpkin, R., & Speer, K. (2007). Global ocean meridional overturning. *Journal of Physical Oceanography*, *37*(10), 2550–2562.
Mazloff, M. R., Heimbach, P., & Wunsch, C. (2010). An eddy-permitting Southern Ocean state estimate. *Journal of Physical Oceanography*, *40*(5), 880–899.
McDougall, T. J., & Barker, P. M. (2011). Getting started with TEOS-10 and the Gibbs Seawater (GSW) Oceanographic Toolbox. *SCOR/IAPSO WG*, *127*, 1–28.
McDougall, T., Jackett, D., Millero, F., Pawlowicz, R., & Barker, P. (2012). A global algorithm for estimating absolute salinity. *Ocean Science*, *8*(6), 1123–1134.
Meijers, A., Bindoff, N., & Rintoul, S. (2011). Estimating the four-dimensional structure of the Southern Ocean using satellite altimetry. *Journal of Atmospheric and Oceanic Technology*, *28*(4), 548–568.
Moreau, S., Penna, A. D., Llort, J., Patel, R., Langlais, C., Boyd, P. W., et al. (2017). Eddy-induced carbon transport across the Antarctic Circumpolar Current. *Global Biogeochemical Cycles*, *31*, 1368–1386. https://doi.org/10.1002/2017GB005669
Morrow, R., Donguy, J.-R., Chaigneau, A., & Rintoul, S. R. (2004). Cold-core anomalies at the subantarctic front, south of Tasmania. *Deep Sea Research Part I: Oceanographic Research Papers*, *51*(11), 1417–1440.
Morrow, R., Fang, F., Fieux, M., & Molcard, R. (2003). Anatomy of three warm-core Leeuwin Current eddies. *Deep Sea Research Part II: Topical Studies in Oceanography*, *50*(12-13), 2229–2243.
Okubo, A. (1970). Horizontal dispersion of floatable particles in the vicinity of velocity singularities such as convergences, pp.445–454.
Pegliasco, C., Chaigneau, A., & Morrow, R. (2015). Main eddy vertical structures observed in the four major eastern boundary upwelling systems. *Journal of Geophysical Research: Oceans*, *120*, 6008–6033.https://doi.org/10.1002/2015JC010950
Petersen, M. R., Williams, S. J., Maltrud, M. E., Hecht, M. W., & Hamann, B. (2013). Athree-dimensional eddy census of a high-resolution global ocean simulation. *Journal of Geophysical Research: Oceans*, *118*, 1759–1774. https://doi.org/10.1002/jgrc.20155
Phillips, H. E., & Rintoul, S. R. (2000). Eddy variability and energetics from direct current measurements in the Antarctic Circumpolar Current south of Australia. *Journal of Physical Oceanography*, *30*(12), 3050–3076.
Pilo, G. S., Oke, P. R., Rykova, T., Coleman, R., & Ridgway, K. (2015). Do east Australian current anticyclonic eddies leave the Tasman Sea? *Journal of Geophysical Research: Oceans*, *120*, 8099–8114. https://doi.org/10.1002/2015JC011026
Rintoul, S. R., & Bullister, J. L. (1999). A late winter hydrographic section from Tasmania to Antarctica. *Deep Sea Research Part I: Oceanographic Research Papers*, *46*(8), 1417–1454.
Rintoul, S, Hughes, C., & Olbers, D. (2001). The Antarctic Circumpolar Current system, pp.271–302.
Rintoul, S. R., & Naveira Garabato, A. (2013). Dynamics of the Southern Ocean circulation. *International Geophysics*, *103*, 471–492.
Rintoul, S. R., & Sokolov, S. (2001). Baroclinic transport variability of the Antarctic Circumpolar Current south of Australia (WOCE repeat section SR3). *Journal of Geophysical Research*, *106*(C2), 2815–2832.
Roemmich, D., & Gilson, J. (2009). The 2004–2008 mean and annual cycle of temperature, salinity, and steric height in the global ocean from the Argo Program. *Progress in Oceanography*, *82*(2), 81–100.
Sallee, J.-B., Speer, K., & Rintoul, S. (2011). Mean-flow and topographic control on surface eddy-mixing in the Southern Ocean. *Journal of Marine Research*, *69*(4-5), 753–777.
Sokolov, S., & Rintoul, S. R. (2009). Circumpolar structure and distribution of the Antarctic Circumpolar Current fronts: 1. Mean circumpolar paths. *Journal of Geophysical Research*, *114*, C11018. https://doi.org/10.1029/2008JC005108
Sun, C., & Watts, D. R. (2001). A circumpolar gravest empirical mode for the Southern Ocean hydrography. *Journal of Geophysical Research*, *106*(C2), 2833–2855.
Swart, N. C., Ansorge, I. J., & Lutjeharms, J. R. (2008). Detailed characterization of a cold Antarctic eddy. *Journal of Geophysical Research*, *113*, C01009. https://doi.org/10.1029/2007JC004190
Swart, S., Speich, S., Ansorge, I. J., & Lutjeharms, J. R. (2010). An altimetry-based gravest empirical mode south of Africa: 1. Development and validation. *Journal of Geophysical Research*, *115*, C03002. https://doi.org/10.1029/2009JC005299
Tamsitt, V., Drake, H. F., Morrison, A. K., Talley, L. D., Dufour, C. O., Gray, A. R., et al. (2017). Spiraling pathways of global deep waters to the surface of the Southern Ocean. *Nature Communications*, *8*(1), 172.
Thompson, A. F., & NaveiraGarabato, A. C. (2014). Equilibration of the Antarctic Circumpolar Current by standing meanders. *Journal of Physical Oceanography*, *44*(7), 1811–1828.

Thompson, A. F., & Sallée, J.-B. (2012). Jets and topography: Jet transitions and the impact on transport in the Antarctic Circumpolar Current. *Journal of Physical Oceanography*, *42*(6), 956–972.

Volkov, D. L., Fu, L.-L., & Lee, T. (2010). Mechanisms of the meridional heat transport in the Southern Ocean. *Ocean Dynamics*, *60*(4), 791–801.

Watts, D. R., Tracey, K. L., Donohue, K. A., & Chereskin, T. K. (2016). Estimates of eddy heat flux crossing the Antarctic Circumpolar Current from observations in Drake Passage. *Journal of Physical Oceanography*, *46*(7), 2103–2122.

Weiss, J. (1991). The dynamics of enstrophy transfer in two-dimensional hydrodynamics. *Physica D: Nonlinear Phenomena*, *48*(2-3), 273–294.